A performance study of NURBS-based isogeometric analysis for interior two-dimensional time-harmonic acoustics

Laurens Coox[a,*], Elke Deckers[a], Dirk Vandepitte[a], Wim Desmet[a]

[a]*KU Leuven, Department of Mechanical Engineering, Celestijnenlaan 300 box 2420, B-3001 Leuven, Belgium*

Abstract

This work evaluates the performance of a NURBS-based isogeometric finite element formulation for solving stationary acoustic problems in two dimensions. An initial assessment is made by studying eigenvalue problems for a square and a circular domain. The spectral approximation properties of NURBS functions of varying order are compared to those of conventional polynomials and are found to be superior, yielding more accurate representations of eigenvalues as well as eigenmodes. The higher smoothness of NURBS shape functions yields better approximations over an extended frequency range when compared to conventional polynomials. Two numerical case studies, including a geometrically complex domain, are used to benchmark the method versus the traditional finite element method. A convergence analysis confirms the higher efficiency of the isogeometric method on a per-degree-of-freedom basis. Simulations over a wider frequency range also illustrate that the method suffers less from the dispersion effects that deteriorate the acoustic response towards higher frequencies. The tensor product structure of NURBS, however, also imposes practical considerations when modelling a complex geometry consisting of multiple patches.

Keywords: time-harmonic acoustics, Helmholtz problem, isogeometric analysis, finite elements, NURBS

1. Introduction

Due to ever tightening regulations on noise emission and exposure to vibration levels, the vibro-acoustic behaviour has become a key factor in product design in recent years. Even more so because of the current trend towards lighter and more energy-efficient designs, which through their lower weight lead to deteriorated noise and vibration properties. Furthermore, the acoustic character of a product has become an important commercial feature that is often

*Corresponding author. Tel.: +32 16 32 28 47.
Email address: Laurens.Coox@mech.kuleuven.be (Laurens Coox)

Post-print accepted by Comput. Methods Appl. Mech. Engrg. *March 4, 2016*
Publisher's version available at http://dx.doi.org/10.1016/j.cma.2016.03.007.

linked to a quality assessment of the entire design. These strong legislative and commercial requirements together with the availability of ever more performant computer systems have made Computer Aided Engineering (CAE) techniques indispensable to design engineers. These techniques enable the prediction of product performance with good accuracy, even in the early design stages. Current state-of-the-use CAE tools for deterministic modelling of acoustic problems are the Finite Element Method (FEM) [1, 2] and the Boundary Element Method (BEM) [3, 4]. These element-based techniques are mostly limited to lower frequency ranges; as the frequency increases, non-deterministic effects become more important, making probabilistic methods such as geometrical acoustics [5] and Statistical Energy Analysis (SEA) [6] much more suited for modelling high-frequency problems. This paper focuses on deterministic methods.

Although CAE has led to significantly shorter design cycles, there is still a lot of room for improvement. Geometric representations in Computer Aided Design (CAD) and the FEM are very different and mostly incompatible with each other. Whereas CAD geometries are spline-based, FE representations are (typically linear) polynomial approximations of the exact CAD geometry. Because the accuracy of the numerical results relies heavily on the FE mesh regularity, this incompatibility requires a tedious and time-consuming meshing step to obtain a suitable (but still approximative) geometry. Despite the multitude of powerful mesh generation algorithms that exist nowadays [7], this meshing process can form a real bottleneck, taking up to 80 % of the total analysis time [8]. Moreover, if mesh refinement is required, the necessary communication with the CAD model is often difficult and sometimes not even possible. Especially for problems of industrial complexity, where optimisation iterations are required, this gap between CAD and CAE can drastically slow down product development cycles. In a geometrical optimisation context, having the exact geometry available can be crucial — especially for acoustic problems towards higher frequencies. Moreover, the parametrised definition of spline-based geometries perfectly lends itself to more efficient representations of the design space. Motivated by this, several papers have already investigated isogeometric shape optimisation, e.g. [9, 10]. Because CAD geometries are typically surface representations, there is a strong and direct link between boundary element formulations and isogeometric approaches. This makes isogeometric BEM frameworks especially attractive [11–14], in particular for geometry optimisation procedures, as exploited in e.g. [15].

A second drawback of the FEM lies in the numerical dispersion effect and its performance towards higher frequencies. As the frequency of interest increases, the number of elements required to limit the pollution errors increases more than linearly [16–18]. These numerical pollution errors introduce a frequency shift in the acoustic response. This restricts the frequency range for which a given FE model can be used to accurately represent the solution and it even introduces an upper frequency limit above which the computational cost becomes prohibitive for the use of the FEM. Pollution errors originate mainly from the use of simple polynomial shape functions, and can be reduced by enriching the field variable approximation with a priori known information about the dynamic solution.

This is done in e.g. multiscale approaches or in generalised FE methods [19]. Also Trefftz-based approaches like the Wave Based Method (WBM) [20] or the Variational Theory of Complex Rays (VTCR) [21] allow much better approximation properties than classical piecewise-polynomial spaces, by employing oscillating basis functions that inherently satisfy the Helmholtz equation.

This paper investigates the use of IsoGeometric Analysis (IGA) [8, 22] as an alternative to the FEM in acoustic problems. IGA is a generalisation of the FEM that aims at bridging the gap between design and analysis by introducing CAD descriptions into a CAE environment. The conventional element-based discretisation and the associated (usually low-order polynomial) shape function expansions are replaced by CAD-based mappings and associated functions, typically spline-based ones. IGA is still an element-based approach with piecewise-polynomial shape functions and as such does not remove the upper frequency limit introduced by the dispersion effect. But the favourable approximation characteristics of spline-based basis functions, such as the higher inter-element continuity, can increase the computational efficiency and alleviate the frequency limitations. The first implementations of IGA [8] were based on Non-Uniform Rational B-Splines (NURBS), one of the most widely used computational geometry representations in engineering designs. Mathematical studies of IGA formulations were presented in [23, 24] and NURBS have been shown to possess intrinsic advantages for analysis purposes [25]. IGA has already attained excellent results in various fields of study, as illustrated by the overview given in [26]. Also acoustic problems have been studied, within BEM frameworks, in [12] using a T-spline-based direct collocational formulation and in [27] using an indirect variational approach. However, employing the isogeometric paradigm in a finite element formulation for time-harmonic acoustic problems remains mostly uncharted territory, except for some preliminary studies by Hughes et al. investigating isogeometric formulations of Helmholtz problems [25, 28, 29]. This research was, however, mostly restricted to either purely eigenvalue analyses or one-dimensional problems.

This paper studies the performance of a NURBS-based isogeometric finite element formulation for solving two-dimensional time-harmonic acoustics and compares it to the conventional FEM. The remainder of the text is structured as follows. First, the mathematical formulation of the acoustic problems under study is given. Section 3 then introduces the preliminaries concerning NURBS-based IGA. After that, numerical examples are presented: Section 4 first illustrates the intrinsic quality of NURBS approximations for two-dimensional Helmholtz problems by studying the eigenvalues and -modes for simple domains in which analytical solutions are available. Two numerical verification case studies are presented in section 5 to assess the performance for the boundary value problem. The paper ends with some concluding remarks.

2. Time-harmonic acoustics in two dimensions

Consider a general interior steady-state acoustic problem as depicted in fig. 1. The acoustic domain Ω is filled with an acoustic fluid characterised by its speed

of sound c and its fluid mass density ρ_0. Assuming a harmonic time-dependency (i.e. $p_a(\boldsymbol{r},t) = p_a(\boldsymbol{r})\mathrm{e}^{\mathrm{j}\omega t}$), the steady-state dynamic behaviour in this acoustic domain is described by the scalar acoustic pressure field $p_a(\boldsymbol{r})$, which is governed by the Helmholtz equation [30]:

$$\boldsymbol{\nabla}^2 p_a(\boldsymbol{r}) + k^2 p_a(\boldsymbol{r}) = -\mathrm{j}\rho_0\omega q_a(\boldsymbol{r}), \qquad \boldsymbol{r} \in \Omega, \tag{1}$$

where $\boldsymbol{r}$ is the position vector, ω the angular frequency, $k = \frac{\omega}{c}$ the acoustic wavenumber, and $q_a(\boldsymbol{r})$ the volumetric source strength distribution. This last term represents internal excitations of the domain, such as acoustic point sources. The term $\boldsymbol{\nabla}^2\bullet = \frac{\partial^2\bullet}{\partial x^2} + \frac{\partial^2\bullet}{\partial y^2}$ is the Laplacian operator, and j denotes the imaginary unit ($\mathrm{j}^2 = -1$). Often the frequency $f = \frac{\omega}{2\pi} = \frac{kc}{2\pi}$ or the acoustic wavelength $\lambda = \frac{2\pi}{k} = \frac{c}{f}$ is used instead of the wavenumber k or angular frequency ω when describing the problem.

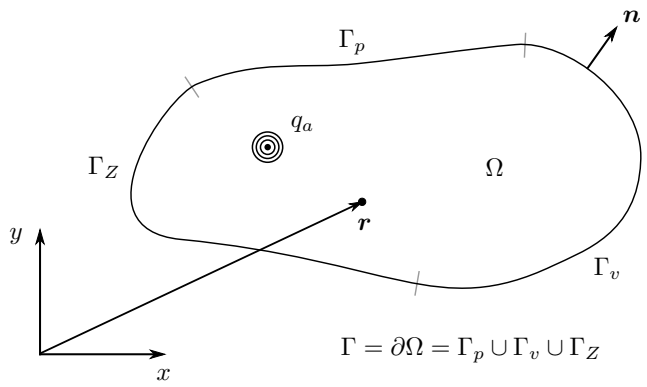

Figure 1: Description of a general two-dimensional interior acoustic problem.

In order to have a unique solution, the Helmholtz equation (1) requires one imposed boundary condition at each point on the problem boundary $\Gamma = \partial\Omega$. This boundary can be divided into three non-overlapping parts, assuming three types of common acoustic boundary conditions: $\Gamma = \Gamma_p \cup \Gamma_v \cup \Gamma_Z$. These are the Dirichlet, Neumann and Robin boundaries, respectively. The boundary conditions on Γ can then be written as follows:

$$p_a(\boldsymbol{r}) = \bar{p}_a(\boldsymbol{r}) \qquad \boldsymbol{r} \in \Gamma_p, \tag{2a}$$

$$\frac{\mathrm{j}}{\rho_0\omega}\frac{\partial p_a(\boldsymbol{r})}{\partial n} = \bar{v}_n(\boldsymbol{r}) \qquad \boldsymbol{r} \in \Gamma_v, \tag{2b}$$

$$\frac{\mathrm{j}}{\rho_0\omega}\frac{\partial p_a(\boldsymbol{r})}{\partial n} = \frac{p_a(\boldsymbol{r})}{\bar{Z}_n(\boldsymbol{r})} \qquad \boldsymbol{r} \in \Gamma_Z. \tag{2c}$$

The quantities $\bar{p}_a$, $\bar{v}_n$ and $\bar{Z}_n$ are the imposed pressure, imposed normal velocity and imposed normal impedance, respectively. The vector $\boldsymbol{n}$ is the outward facing

unit normal on the boundary. The Helmholtz equation (1) together with the boundary conditions (2) fully define the acoustic pressure field $p_a(\boldsymbol{r})$ in the entire problem domain Ω.

3. NURBS-based isogeometric analysis for acoustics

This section introduces the terminology and formulae regarding NURBS surfaces and their corresponding basis functions in the context of IGA. First the construction of NURBS from B-splines is discussed. Then their use in acoustic isogeometric analysis as well as their features of importance in this work are examined. A more detailed explanation about IGA can be found in [8, 22] and about NURBS in particular in [31].

3.1. From B-spline bases to NURBS surfaces

NURBS are built starting from B-splines. A set of B-splines of polynomial order p is defined by a knot vector $\boldsymbol{\Xi} = [\xi_1, \xi_2, \ldots, \xi_{n+p+1}]$. This is a sequence of non-decreasing coordinates in the parameter space ξ, where $\xi_k \in \mathbb{R}$ $(k = 1, 2, \ldots, n+p+1)$ with n the number of basis functions forming the B-spline. Open knot vectors, where the first and the last knot each have a multiplicity of $p+1$, are standard in CAD. Starting from a knot vector, B-spline basis functions $N_i^p(\xi)$ $(i = 1, \ldots, n)$ are defined recursively using the Cox – de Boor recursion formula [32, 33]:

$$\begin{aligned} p = 0: \quad & N_i^0(\xi) = \begin{cases} 1 & \xi_i \leq \xi < \xi_{i+1} \\ 0 & \text{otherwise} \end{cases}, \\ p > 0: \quad & N_i^p(\xi) = \frac{\xi - \xi_i}{\xi_{i+p} - \xi_i} N_i^{p-1}(\xi) + \frac{\xi_{i+p+1} - \xi}{\xi_{i+p+1} - \xi_{i+1}} N_{i+1}^{p-1}(\xi). \end{aligned} \tag{3}$$

These functions are piecewise polynomial.

By assigning a weight w_i to every B-spline function, a NURBS basis can be generated. The NURBS basis functions $R_i^p(\xi)$ of polynomial order p are then given by

$$R_i^p(\xi) = \frac{N_i^p(\xi) w_i}{W(\xi)} = \frac{N_i^p(\xi) w_i}{\sum_{i_w=1}^{n} N_{i_w}^p(\xi) w_{i_w}} \quad \text{with} \quad i = 1, \ldots, n, \tag{4}$$

with $W(\xi)$ the weighting function. Each $R_i^p(\xi)$ is a piecewise rational function, since $N_i^p(\xi)$ and $W(\xi)$ are both piecewise polynomial. If all the weights are equal, then $R_i^p(\xi) = N_i^p(\xi)$: the basis functions are no longer rational and the NURBS degenerates into a B-spline. B-splines are therefore a subset of NURBS.

Multivariate NURBS entities are generated by taking the tensor product of univariate NURBS bases. Given two polynomial orders p and q, and a pair of knot vectors $\boldsymbol{\Xi} = [\xi_1, \xi_2, \ldots, \xi_{n+p+1}]$ and $\boldsymbol{H} = [\eta_1, \eta_2, \ldots, \eta_{m+q+1}]$, a bivariate NURBS basis is defined as

$$R_{i,j}^{p,q}(\xi, \eta) = \frac{N_i^p(\xi) M_j^q(\eta) w_{i,j}}{\sum_{i_w=1}^{n} \sum_{j_w=1}^{m} N_{i_w}^p(\xi) M_{j_w}^q(\eta) w_{i_w, j_w}} \quad \text{with} \quad \begin{matrix} i = 1, \ldots, n \\ j = 1, \ldots, m, \end{matrix} \tag{5}$$

where $N_i^p(\xi)$ and $M_j^q(\eta)$ represent univariate B-spline basis functions of order p and q, associated with knot vectors $\boldsymbol{\Xi}$ and $\boldsymbol{H}$, respectively. To obtain a NURBS surface geometry $\mathbf{S}(\xi,\eta)$, a linear combination of these basis functions is made using a net of vector-valued weighting coefficients $\mathbf{B}_{i,j} \in \mathbb{R}^{\mathrm{d}}$ called control points:

$$\mathbf{S}(\xi,\eta) = \sum_{i=1}^{n}\sum_{j=1}^{m} R_{i,j}^{p,q}(\xi,\eta)\mathbf{B}_{i,j}. \tag{6}$$

It is worth noting that the control points are not necessarily interpolatory, i.e. they do not lie on the surface they define.

Equation (6) represents a single NURBS surface patch, but for generating more complex geometries, several interconnected patches are usually required — so-called *multipatch* surfaces.

3.2. NURBS in an isogeometric finite element formulation for acoustics

By invoking the isoparametric concept, the mapping of the NURBS basis in eq. (5) can be used in a shape function expansion much in the same way as it is done in the conventional FEM. The acoustic pressure field can then be approximated as

$$p_a(\boldsymbol{r}) \approx \hat{p}_a(\boldsymbol{r}) = \sum_{k=1}^{n_d} N_k(\boldsymbol{r}) \cdot d_k = \mathbf{N}\boldsymbol{d} \qquad \boldsymbol{r} \in \Omega, \tag{7}$$

where $\boldsymbol{d}$ is the $n_d \times 1$ vector of unknowns collecting the control variables or Degrees Of Freedom (DOFs) d_k, and $\mathbf{N}$ the $1 \times n_d$ vector containing the NURBS basis functions $N_k(\boldsymbol{r})$ of the acoustic surface geometry under study. Employing this shape function expansion in the weak form of Galerkin's weighted residuals formulation of the Helmholtz problem described by eqs. (1) and (2) yields a linear system of equations that can be written in matrix form:

$$\left(\mathsf{K} + \mathrm{j}\omega\mathsf{C} - \omega^2\mathsf{M}\right)\boldsymbol{d} = \boldsymbol{F_a}, \tag{8}$$

where K, C and M are the stiffness, damping and mass matrix, respectively, and $\boldsymbol{F_a}$ an acoustic force vector. These arrays are defined as follows (using row index i and column index j):

$$K_{ij} = \int_{\Omega} \left(\boldsymbol{\nabla} N_i(\boldsymbol{r}) \cdot \boldsymbol{\nabla} N_j(\boldsymbol{r})\right) \mathrm{d}\Omega, \tag{9}$$

$$C_{ij} = \int_{\Gamma_Z} \left(\frac{\rho_0}{\bar{Z}_n} N_i(\boldsymbol{r}) N_j(\boldsymbol{r})\right) \mathrm{d}\Gamma, \tag{10}$$

$$M_{ij} = \int_{\Omega} \left(\frac{1}{c^2} N_i(\boldsymbol{r}) N_j(\boldsymbol{r})\right) \mathrm{d}\Omega, \tag{11}$$

$$F_{a,i} = \int_{\Gamma_v} \left(-\mathrm{j}\rho_0\omega N_i(\boldsymbol{r})\bar{v}_n\right) \mathrm{d}\Gamma + \int_{\Omega} \left(N_i(\boldsymbol{r}) q_a(\boldsymbol{r})\right) \mathrm{d}\Omega. \tag{12}$$

The prescribed pressure, i.e. Dirichlet boundary condition (2a), still needs to be enforced. This is straightforwardly done in the case of a homogeneous prescribed pressure by directly applying the prescribed pressure values to the control variables. Inhomogeneous Dirichlet conditions, however, require more care due to the non-interpolatory nature of the basis functions. The boundary conditions must be approximatively satisfied using functions lying in the employed NURBS space, e.g. by means of a least-squares best-fit.

The arrays in eq. (8) can be assembled via the same procedure as in the conventional FEM. The matrices are sparse and symmetrical, and, assuming a proper numbering of the DOFs, have a banded structure. This allows the use of efficient matrix solvers. Moreover, the mass and stiffness matrix are frequency-independent, and so is the damping matrix if the prescribed normal impedance does not depend on frequency. In that case the system matrices can be reused for calculating multiple frequency lines. While the elements of the mass and stiffness matrices are always real-valued, those of the damping matrix are usually complex because the imposed normal impedance is typically complex.

Following remarks can be made for a NURBS-based isogeometric framework:

- The mesh for a NURBS patch results from the tensor product of the underlying knot vectors: the mapped knot spans divide the problem domain into elements. A NURBS basis function of order p always has a support of $p+1$ knot spans (including repeated knots) in one dimension, which is much larger for higher orders as compared to classical FEM functions. However, this does not lead to an increased matrix bandwidth. In fact, the total number of functions that any given shape function can share support with is no more than $2p+1$ (itself included) regardless of whether the basis is a NURBS or a traditional FE basis, as illustrated for quadratic functions in fig. 2. The resulting system matrices therefore have the same bandwidth, and solving them requires a similar computational cost for both IGA and the FEM with a given number of DOFs of a given polynomial order. In spite of this similar solving cost, the matrix assembly will be more expensive for IGA. This is due to the wider support of the NURBS basis functions as compared to the FEM, which constructs shape functions per element. However, especially in applications like time-harmonic acoustics, where typically a wide frequency range is studied and where the system matrices can be reused for calculations at different frequencies, (repeatedly) solving the system of equations is more of a bottleneck than the (one-off) matrix assembly. This is the reason why it can be considered valuable and meaningful to compare the performance of IGA and FE models on a per-DOF basis, even though the true basis of comparison should be computational cost and not DOFs.

- Across a knot, the basis functions have a C^{p-m} continuity, with m the multiplicity of the knot. NURBS bases are therefore quite flexible regarding inter-element continuity, and virtually arbitrarily high continuities can be obtained. Being a second-order problem, the Helmholtz equation only

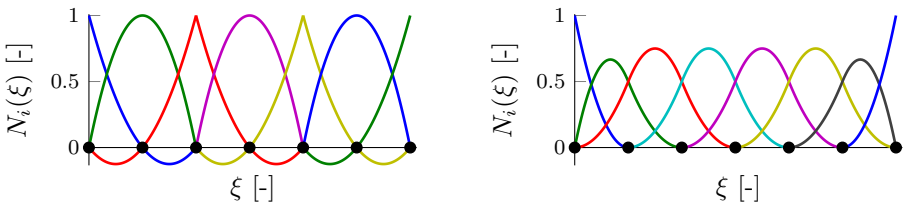

(a) Quadratic polynomial shape functions for equally spaced nodes.

(b) Quadratic NURBS shape functions $N_i^2(\xi)$ as defined in eq. (3), using a uniform open knot vector.

Figure 2: One-dimensional quadratic shape functions for a mesh consisting of seven nodes (indicated by •) using (a) conventional polynomials and (b) NURBS.

requires C^0 continuity, but this higher smoothness of NURBS can nonetheless increase the computational accuracy as compared to conventional C^0-continuous finite elements [25].

- Mesh refinement can be done by knot insertion and by order elevation. These procedures enable conventional h- and p-refinement, but there is also an additional possibility called k-refinement. This technique first increases the polynomial order and then inserts knots, which also increases the smoothness of the basis and has no analogue in traditional FEM approaches [8].

- Multiple NURBS patches are by default not continuous at the borders, but compatibility in multipatch geometries is typically obtained by employing the same NURBS discretisation on both sides of patch interfaces. Because of the tensor product structure, this means that mesh refinement propagates from patch to patch. Even in single patches, local refinement is not inherently possible because of this tensor product structure. There are techniques to alleviate these restrictions [34–37] but they require extra treatment. Another option is to use spline descriptions that inherently allow for local refinement, such as T-splines [38–40].

- Because the control variables are in general not interpolated by the basis functions, their values do not represent nodal values of the solution, in contrast to traditional FEM DOFs. This also means that the control mesh (i.e. the grid of the control points) is in general not the same as the element mesh (i.e. the grid formed by the mapping of the knot vectors).

- The fact that even the most coarse geometry description is an exact one can be exploited in isogeometric analysis by using non-isoparametric approaches, thus avoiding the use of redundant data [41]. Or consider a situation where the original CAD geometry is very finely discretised, (much) finer than the field variable discretisation requires for an accurate solution. This is very common for CAD files of industrial complexity. In

that case, choosing independent discretisation schemes for geometry and field variables could be computationally more efficient. This also holds for applications where the geometric basis functions are not well-suited for approximating a particular solution [42], for instance when the solution is non-smooth but the geometry is.

4. The intrinsic quality of a NURBS basis for Helmholtz problems

This section studies the potential of NURBS as basis functions as compared to traditional polynomials for a better representation of these higher frequency pressure fields governed by the Helmholtz equation. NURBS-based isogeometric formulations have already been shown to exhibit advantageous properties for analysis purposes as compared to FEM, in particular with respect to spectral approximation properties [25, 28, 29]. In [25] Hughes et al. study this in particular also for elliptic problems by analysing the variational form of Poisson's equation. They conclude that the poor representation of higher eigenmodes is not an issue for such problems, because those modes do not contribute significantly to the solution. This is true, but it is not the entire story for all elliptic problems. In the case of the Helmholtz equation (1), the wavenumber of analysis is also of importance — Poisson's problem is a special case of the Helmholtz problem with zero wavenumber. Higher modes usually do not participate strongly in the solution at lower wavenumbers and the poor representation is in that case indeed not of major concern. At higher frequencies, however, the higher modes may dominate the response. With increasing frequency, the mesh needs to become increasingly finer in order to improve the numerical representation of these modes. This limits the frequency range that can be studied with a given model and makes the representation of the higher eigenmodes important for stationary acoustics and for dynamic problems in general.

The solution accuracy is determined by the accuracy of the eigenfrequencies and -modes of the system matrices. If this accuracy can be conserved towards higher frequencies, the frequency response of a system can be calculated more efficiently. It will be shown that IGA can in that sense alleviate the mesh requirements. Both eigenfrequencies and eigenmodes are studied for simple square and circular problem domains, for which analytical solutions exist. As the eigenfrequencies have already been studied to some extent in other works [25, 28, 29], this paper mainly focuses on the eigenmodes. In contrast to these other works, the analysis of the circular domain also allows to assess the influence of the geometrical error present in the FEM approximations. All the IGA simulations in this work are carried out in MATLAB with an in-house code based on the GeoPDEs framework [43], and the FEM simulations with the commercial software COMSOL Multiphysics [44].

4.1. Square domain

Consider an acoustic fluid with unit density and speed of sound in a unit square domain with zero pressure boundary conditions. The governing equations

are then:

$$\begin{aligned} &\boldsymbol{\nabla}^2 p_a(x,y) + k^2 p_a(x,y) = 0, \qquad (x,y) \in \Omega = [0,1]\,\mathrm{m} \times [0,1]\,\mathrm{m}, \\ &p_a(x,y)\Big|_{\partial\Omega} = 0. \end{aligned} \tag{13}$$

The solution for this problem can be analytically calculated [45] and yields the following description for the exact natural wavenumbers k_{mn} and mode shapes u_{mn}:

$$k_{mn} = \pi\sqrt{m^2+n^2}, \qquad m,n = 1,2,3,\ldots, \tag{14}$$

$$u_{mn}(x,y) = U_{mn}\sin(m\pi x)\sin(n\pi y), \qquad m,n = 1,2,3,\ldots, \tag{15}$$

with U_{mn} a scaling factor. These analytical results are compared to numerical solutions obtained using different orders of shape functions.

4.1.1. Eigenvalues

In [28, 29] the numerical eigenfrequencies using NURBS-based IGA models of varying polynomial order are studied (both in 1D and in 2D with largely analogous results) and it is found that the specific parametrisation used is of great importance. For the detailed study the reader is referred to [28], but its main conclusion of interest for the current work is that by using a uniformly sized net of control points (as in fig. 3a) instead of uniformly sized elements (as in fig. 3b), a more accurate discrete eigenfrequency spectrum can be obtained. The use of uniformly spaced control points results in a non-linear parametrisation instead of a linear[1] one. Although it is the more straightforward option, a linear parametrisation in this case leads to so-called *optical branches* in the upper part of the eigenfrequency spectrum: spurious discontinuities in the spectrum which result in large errors in the higher eigenfrequencies.

As the discrete eigenfrequency spectra for these two discretisations have already been extensively treated in [28], they will not again be compared at length here. Only the better performing version with uniformly spaced control points (fig. 3a) is studied. Figure 4a shows this mesh's normalised eigenwavenumber spectrum (which is the same as the normalised eigenfrequency spectrum here) for both FE and IGA models of varying polynomial order. The vertical axis shows the ratio of the numerical eigenwavenumber k_i versus the corresponding exact one $k_{i,\mathrm{ex}}$. On the horizontal axis, the index i indicates the number of the modes when they are ordered from low to high in wavenumber, with N the total number of DOFs in the system. The quantity i/N is referred to here as the normalised mode index. These curves are obtained using models of approximately 1000 DOFs. It is worth noting that the exact shape of these curves depends on the fineness of the applied discretisation, but that they converge to a shape that characterises the accuracy of the numerical method and of the discretisation topology. Also note that the first-order models give the same results in

[1] The term *linear* here refers to the fact that the Jacobian determinant of the mapping is constant, not to the order of the B-splines used in the parametrisation.

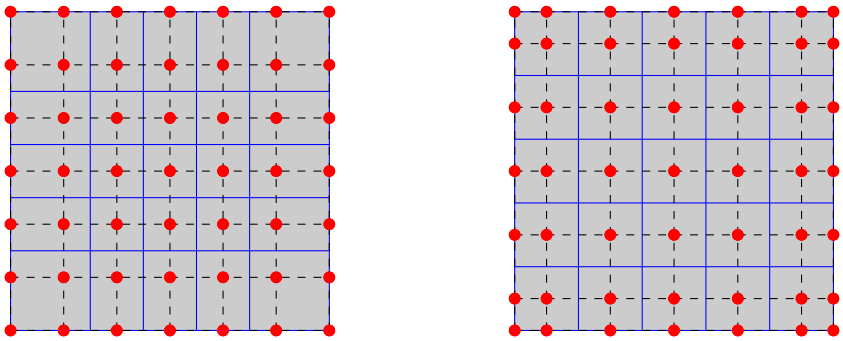

(a) Mesh with a uniformly sized control net (resulting in a non-linear mapping), as proposed in [28].

(b) Mesh with uniformly sized elements (resulting in a linear mapping with a constant Jacobian).

Figure 3: Two types of parametrisations for a square domain (generated using quadratic B-spline basis functions). Solid blue lines delineate the elements, while the dashed black lines form the control net connecting the control points in red.

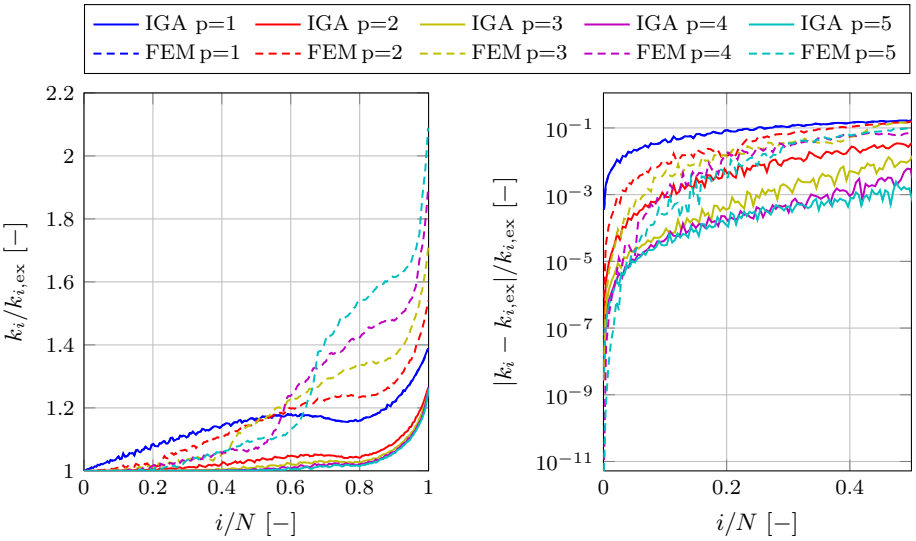

(a) Normalised discrete eigenwavenumber spectrum.

(b) Discrete eigenwavenumber error in the lower part of the spectrum.

Figure 4: Assessment of the accuracy of the discrete eigenwavenumber spectra for a unit square domain obtained using models of varying polynomial order p. The IGA models retain the accuracy of the eigenvalues up to much higher frequencies, allowing the use of IGA toward higher frequencies in comparison to FEM.

both cases, since their shape functions are identical when $p = 1$. Although all the models deteriorate towards higher frequencies, the IGA eigenwavenumbers retain their accuracy far longer than the FEM ones. Moreover, the eigenvalue accuracy for the IGA models converges with increasing polynomial order in the upper part of the spectrum, whereas the curves diverge in the FEM case. To give a clearer picture of the lower frequency performance, fig. 4b shows the relative error of the normalised discrete eigenwavenumbers in the lower part of the spectrum. These curves show that for the lower modes, both IGA and FEM accuracy increase with increasing order and that also for lower wavenumbers the IGA models outperform the FEM ones. In both cases the lower part of the spectrum converges with increasing polynomial order.

It should be noted that the fact that the uppermost part of the eigenfrequency spectrum is more accurately represented for NURBS does not necessarily contribute to higher solution accuracies. In that part of the spectrum, also the IGA eigenvalues already show significant error — too significant to still contribute to the solution accuracy. In practice this means that a given mesh will never be used in its entire spectral range, as the higher modes are too much distorted and have no approximability anyway, as will be shown in the next section. In numerical engineering practice, rules of thumb are used to ensure proper use of numerical models and correct interpretation of the results:

- When using a modal analysis instead of a direct one, all modes with a frequency up to twice the frequency of interest should be included. For this set of modes, that means that the highest valid frequency is the one at a normalised mode index of $i/N = 0.25$.

- For a linear mesh at least 6 elements per wavelength are necessary in order to keep interpolation errors acceptable — and with regard to the pollution error even stricter limitations are necessary toward higher frequencies [16, 18, 46]. Following this rule limits the use of this mesh to a normalised mode index of 0.085, an even stricter limit. The accuracy of the linear discrete spectrum at that point is about 4 %.

These rules of thumb stem from FEM simulations and indicate the region where the linear FE discretisation still yields acceptable results. But thanks to the higher accuracy of the IGA discretisation in the extended lower frequency region, this rule of thumb can be relaxed. For the quadratic IGA discrete spectrum, for instance, a 4 % error is not reached until a normalised mode index of $i/N = 0.55$, while the quadratic FE model already exceeds this error level at $i/N = 0.23$. Nonetheless, the quality of the IGA discretisations is not such that the entire spectrum can contribute to the solution accuracy up to also the very high modes: an upper limit well below the highest eigenfrequency remains. This can be illustrated by the accuracy of the eigenmodes with increasing mode number.

4.1.2. Eigenmodes

The solution error is determined not only by the accuracy of the eigenvalues but also by that of the eigenmodes. A commonly used tool for comparing mode

shapes is the Modal Assurance Criterion (MAC) [47]. The MAC value between two modal vectors $\boldsymbol{u}$ and $\boldsymbol{v}$ is a scalar number relating the degree of consistency between these two vectors and is defined as follows:

$$\mathrm{MAC}(\boldsymbol{u}, \boldsymbol{v}) = \frac{\left|\boldsymbol{u}^H \boldsymbol{v}\right|^2}{\left(\boldsymbol{u}^H \boldsymbol{u}\right)\left(\boldsymbol{v}^H \boldsymbol{v}\right)}, \tag{16}$$

where $\bullet^H$ denotes the Hermitian or complex conjugate transpose. The modal vectors $\boldsymbol{u}$ and $\boldsymbol{v}$ are vectors containing evaluations (in the same points) of the mode shapes under comparison. A large set of evaluation points spread out over the problem domain is used: sufficiently large to avoid aliasing, in this case 4356 points. Typically a MAC matrix is calculated, collecting MAC values between the modes of two given mode sets, again sorted from low to high wavenumber. The MAC can take on values between zero, indicating no consistent similarity between $\boldsymbol{u}$ and $\boldsymbol{v}$, and one, representing a perfect match. Hence, if two mode sets are identical, the diagonal of the MAC matrix comparing them will be a unity diagonal. This does not mean that the MAC matrix should be the identity matrix in case of an exact match: because modal vectors are in general not directly orthogonal (but only mass-orthogonal), the off-diagonal MAC values are not necessarily exactly zero — although they will generally be very close to zero.

In general it is expected that the lower numerical modes show good agreement with the analytical ones, while the higher modes are increasingly less well approximated. The point where this starts to become noticeable, however, comes much sooner for the FEM than for IGA. Figure 5 shows the MAC matrix of the first 150 eigenmodes for a fifth-order FE model compared to the corresponding analytical modes. The total number of DOFs (and thus the total number of modes present) used in this approximation is 196. This means that the modes shown in the MAC matrix go up to three quarters into the normalised spectrum (cf. fig. 4). Although the identity matrix structure is clearly present for the lower modes, mismatches between modes are introduced after mode 30. Increasing the mode number further, beyond 50, the MAC matrix starts to deviate significantly from the identity matrix. This indicates that some modes in the numerical mode set are switched, i.e. they are ordered in a different way, as fig. 6 shows for modes 49 through 52. The 49^{th} FEM mode, for instance, corresponds to the 51^{st} analytical mode, while the 49^{th} analytical mode matches the 50^{th} FEM mode. These mismatches clearly express themselves in fig. 5 through the non-zero off-diagonal values close to one around mode 50. Such switching phenomenon is detrimental to the solution accuracy, as it will introduce a frequency shift in the resulting frequency responses. Also the effect of the shifted eigenfrequencies indicated in fig. 4 already plays a role here. More thorough investigation of the MAC matrix also shows non-zero off-diagonal values that are not close to one but rather close to zero (the grey data in fig. 5). In this particular case of the square domain, these off-diagonal should be zero for a perfect match, since the analytical modal vectors are directly orthogonal here. The non-zero values indicate that some modes overlap to some extent: parts of

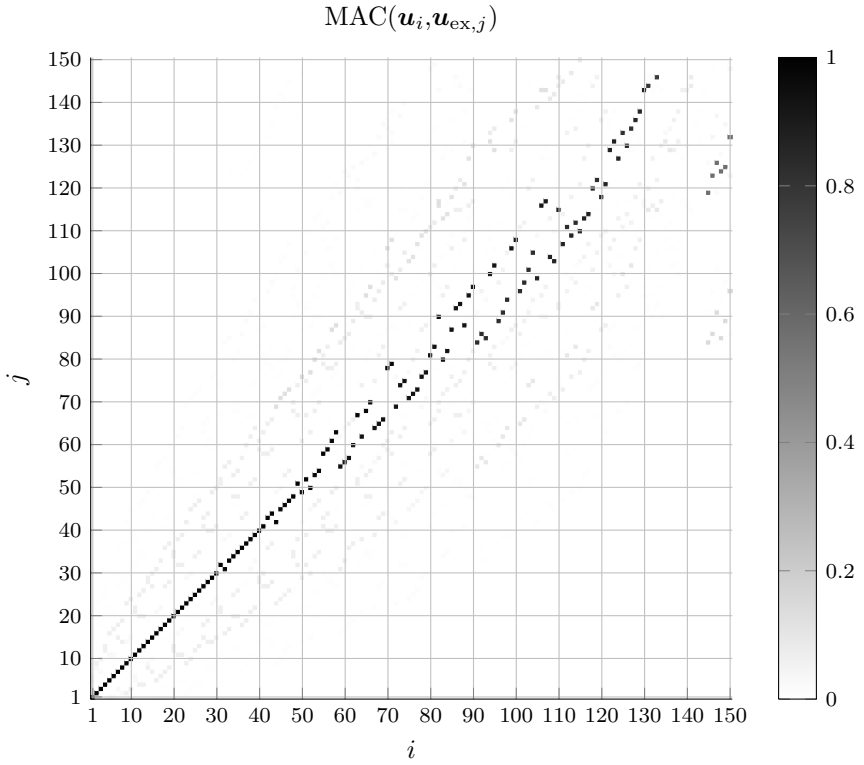

Figure 5: MAC matrix for the first 150 eigenmodes of a unit square domain using fifth-order FEM (horizontal index) compared to the analytical eigenmodes (vertical index). The diagonal structure of the matrix quickly starts to fade above mode 50, representing modes present at incorrect frequencies.

the mode shape correspond between a numerical mode shape and an analytical one, even though they do not represent the same mode.

Figure 7 shows the corresponding MAC matrix when using 196 NURBS functions of fifth order. As already hinted by the good match between the IGA and the analytical mode shapes in fig. 6, the identity matrix structure is clearly retained up to much higher modes than in the FEM case. Only above mode 100 the diagonal structure starts to break down. The off-diagonal elements are less pronounced as well. These MAC matrices highlight that also the mode shapes are represented more accurately up to significantly higher frequencies, and not just the eigenvalues. This confirms that, for a given number of DOFs, an IGA model can calculate frequency responses more accurately over a higher frequency range than an equivalent FE model. MAC matrices obtained when using fifth-order shape functions are shown here, but lower-order analyses indicate the same trend.

For the sake of completeness, fig. 8 also shows the MAC matrix obtained for a

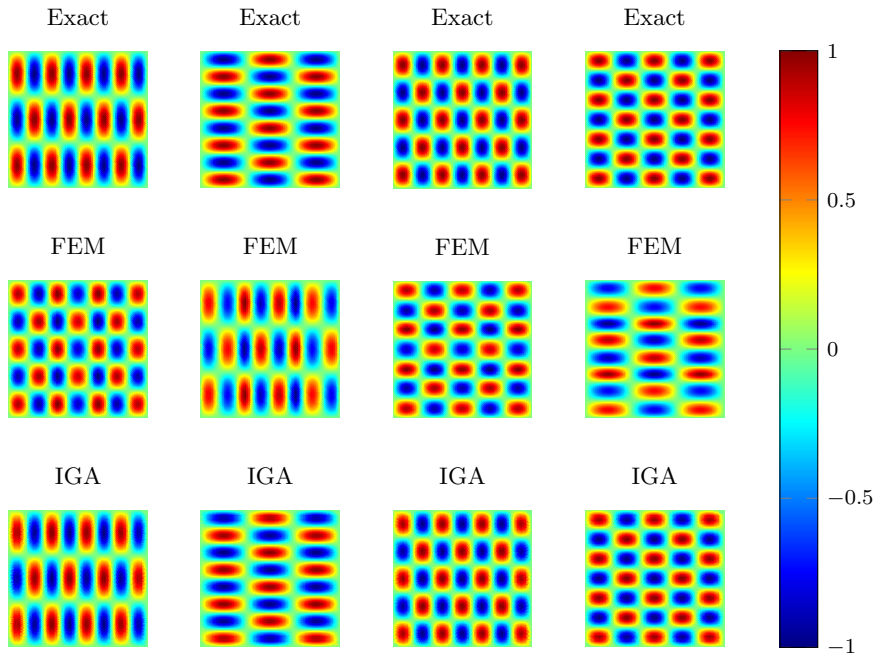

(a) 49^{th} mode $u_{83}(x, y)$ (b) 50^{th} mode $u_{38}(x, y)$ (c) 51^{st} mode $u_{75}(x, y)$ (d) 52^{nd} mode $u_{57}(x, y)$

Figure 6: Analytical mode shapes number 49 through 52, as described by eq. (15), compared to the corresponding numerically calculated modes with both FEM (cf. fig. 5) and IGA (cf. fig. 7). In contrast to the IGA modes, the FEM mode shapes appear in the wrong order.

fifth-order IGA model when using the straightforward linear parametrisation (cf. fig. 3b) instead of the non-linear one (cf. fig. 3a) used in figs. 4 and 7. Although the resulting modes are still more accurate than in the corresponding FEM case, the correspondence with the analytical modes is worse than in fig. 7 — despite the lower off-diagonal values. The importance of the applied discretisation found in [28] based on the accuracy of the eigenvalues is confirmed by these findings based on the eigenmodes' approximability.

4.2. Circular domain

The study carried out in the previous section for the square domain can also be conducted for a circular problem domain. Here, the geometrical error presents an additional disadvantage for the FEM. Indeed, quadratic (and higher-order) NURBS can exactly represent circles, whereas conventional FEM shape functions cannot. Consider a circle of unit radius filled with a fluid with unit properties and with zero pressure boundary conditions. Using a transformation to polar coordinates r and θ and leaving out the (r, θ) dependency of $p_a(r, \theta)$

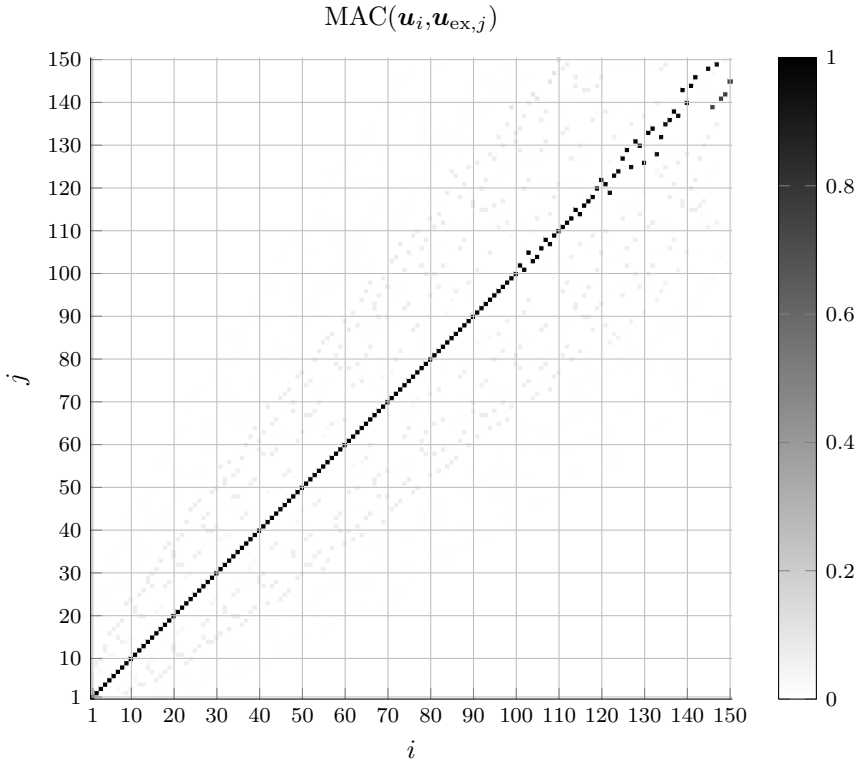

Figure 7: MAC matrix for the first 150 eigenmodes of a unit square domain using fifth-order IGA with uniformly spaced control points (horizontal index) compared to the analytical eigenmodes (vertical index). The match between numerical and exact modes is clearly present up to much higher modes than in the FE model.

for the sake of brevity, the governing equations become:

$$\begin{aligned} &\frac{\partial^2 p_a}{\partial r^2} + \frac{1}{r}\frac{\partial p_a}{\partial r} + \frac{1}{r^2}\frac{\partial^2 p_a}{\partial \theta^2} + k^2 p_a = 0, \qquad (r,\theta) \in \Omega = [0,1]\,\mathrm{m} \times [0, 2\pi[\,, \\ &p_a\Big|_{\partial\Omega} = 0. \end{aligned} \tag{17}$$

The analytical solution for this problem involves Bessel functions of the first kind. The exact eigenwavenumbers k_{mn} and eigenmodes u_{mn} are [45]:

$$k_{mn} = \lambda_{mn}, \qquad m = 0, 1, \ldots,\ n = 1, 2, \ldots, \tag{18}$$

$$u_{mn,\cos}(r,\theta) = U_{mn,\cos} J_m(\lambda_{mn} r)\cos m\theta, \qquad m = 0, 1, \ldots,\ n = 1, 2, \ldots, \tag{19}$$

$$u_{mn,\sin}(r,\theta) = U_{mn,\sin} J_m(\lambda_{mn} r)\sin m\theta, \qquad m = 1, 2, \ldots,\ n = 1, 2, \ldots, \tag{20}$$

with $J_m(\bullet)$ the Bessel function of the first kind and order m, and λ_{mn} the n-th positive root of J_m. The factors $U_{mn,\star}$ are again scaling factors.

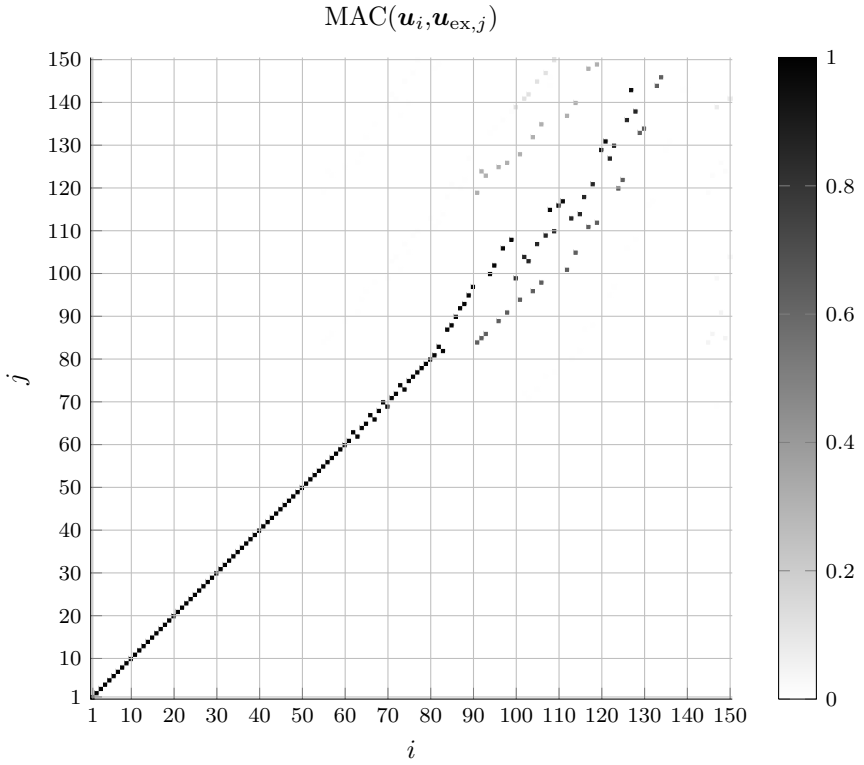

Figure 8: MAC matrix for the first 150 eigenmodes of a unit square domain using fifth-order IGA with uniform elements (horizontal index) compared to the analytical eigenmodes (vertical index). The match between numerical and exact modes is still better than in the FEM case, but worse than when using IGA with uniform control points.

4.2.1. Eigenvalues

Again the performance of IGA calculations is compared to that of conventional FE models. Given the importance of the applied discretisation in the case of the square domain, multiple types of IGA geometry discretisations have been investigated here as well. In particular two types have been studied, as shown in fig. 9: a polar mapping (i.e. where the mesh grid consists of radial and circumferential lines (cf. fig. 9a) and a Cartesian one (i.e. a typical square mesh deformed to a circular shape, cf. fig. 9b). However, no large differences in performance between these isogeometric mappings are found. Although the exact shapes of the discrete spectra are different, both mappings perform similarly without qualitative discrepancies between them. Because the Cartesian mesh (fig. 9b) of the domain was found to perform better overall, only those results are shown here.

Figure 10a shows the normalised discrete eigenwavenumber spectrum for

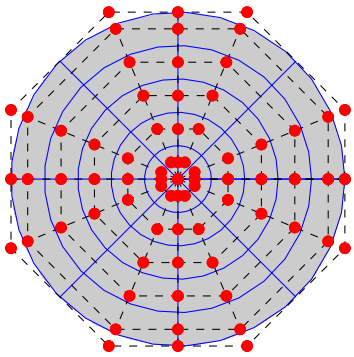

(a) Mesh consisting of a polar mapping, with one parametric coordinate running in the radial direction and the other one tangentially.

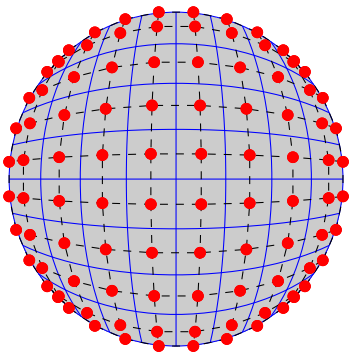

(b) Mesh generated by deforming a square mesh to fit a circular boundary.

Figure 9: Two types of parametrisations for a circular domain (generated using quadratic NURBS basis functions). Solid blue lines delineate the elements, while the dashed black lines form the control net connecting the control points in red.

both IGA and FEM solutions of eq. (17). Calculations are carried out with around 1000 DOFs — the exact number may vary slightly depending on the discretisation in order to generate a good quality mesh. Applying the same rule of thumb of 6 elements per wavelength indicates a validity of the linear models up to a normalised mode index $i/N = 0.055$. In contrast to the square case, now also the IGA curves diverge with increasing order in the upper part of the spectrum. Interesting to notice here is also the difference between the two first-order models. While the linear IGA and the linear FEM simulations yield the same wavenumbers for the lower modes, a discrepancy is introduced above a normalised mode index of about 0.4. Although linear NURBS are identical to linear polynomial shape functions in the FEM, the meshes used here in the two cases are different. In order to obtain a good quality FE mesh to have a fair comparison, triangular elements are used, yielding a different discretisation with different shape functions. In the IGA case, a tensor product mesh needs to be used, yielding quadrilateral elements. This introduces some distorted elements near the boundaries.

Investigation of the higher order discretisations shows that the IGA models outperform the FEM for about the lowest 70 % of the complete set of modes, but after that their performance deteriorates. In fact, the error for the higher IGA wavenumbers becomes very high, yielding completely wrong eigenvalues — even more so than for the square domain. Also the FEM curves show exceedingly large errors for the higher frequencies. Here it should again be noted that this is not necessarily an issue; the same reasoning as for the square domain also holds here: the highest modes anyway have no approximability and do not contribute to the solution accuracy. It is rather because of the higher accuracy in the

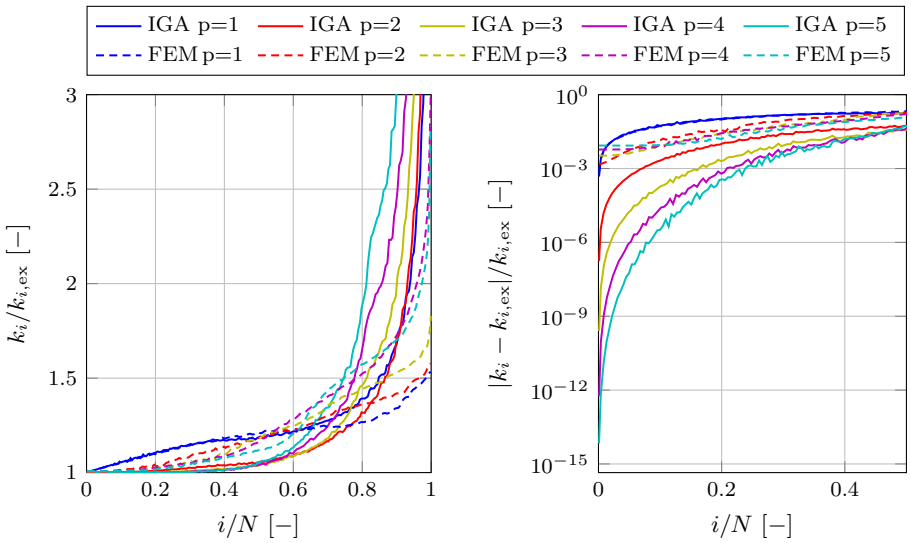

(a) Normalised discrete eigenwavenumber spectrum.

(b) Discrete eigenwavenumber error in the lower part of the spectrum.

Figure 10: Assessment of the accuracy of the discrete eigenwavenumber spectra for the circular domain obtained using models of varying polynomial order p. Even more so than was the case for the square domain, the IGA models retain the accuracy of the eigenvalues up to much higher frequencies. This is partially due to the geometrical error present in the FE models.

extended lower frequency part of the spectrum that IGA discretisations can be used more efficiently up to higher frequencies. Figure 10b shows this better performance for the lower modes more clearly by plotting the eigenwavenumber error on a logarithmic scale.

As the discrete error spectrum shows, the IGA accuracy increases with increasing polynomial order for the lower modes up to about 50 % of the spectrum. The accuracy also strongly increases with decreasing mode index for a given order. In contrast to the IGA models, all the FEM curves stagnate around the same error level for the lowest modes. This was not observed for the square domain (cf. fig. 4b), hinting that this stagnation point is caused by the geometrical error present in the FE discretisations. Representing the circular boundary by a polygon introduces a geometrical error that limits the maximum solution accuracy that can be obtained and that can be characterised by the resulting error on the circular surface area. Discretising a circle of radius R with n_b linear segments of equal length reduces the surface area of the circle by an amount of $(\frac{\pi R^2}{n_b} - \frac{R^2}{2}\sin\frac{2\pi}{n_b})$ for each segment. The total relative error $\epsilon_\circ$ on the surface

area of the circle is then

$$\epsilon_\circ = \frac{\pi R^2 - \dfrac{n_b R^2}{2} \sin \dfrac{2\pi}{n_b}}{\pi R^2} = 1 - \frac{n_b}{2\pi} \sin \frac{2\pi}{n_b}. \tag{21}$$

The linear FE mesh used here consists of 93 boundary segments. This yields a relative surface area error of $7.61 \cdot 10^{-4}$, which can be used as an indicator for the geometrical error inherently present in this discretisation. The lowest mode obtained using this mesh gives a relative error of $7.13 \cdot 10^{-4}$, indicating that the stagnation point of the FEM curves is indeed induced by the geometrical error.

4.2.2. Eigenmodes

Also here the numerically obtained eigenmodes can be compared to the analytical ones in eqs. (19) and (20) using MAC matrices. Figure 11 shows the MAC matrix for the first 150 modes for a second-order FE model compared to the corresponding analytical ones. The total number of DOFs used in this

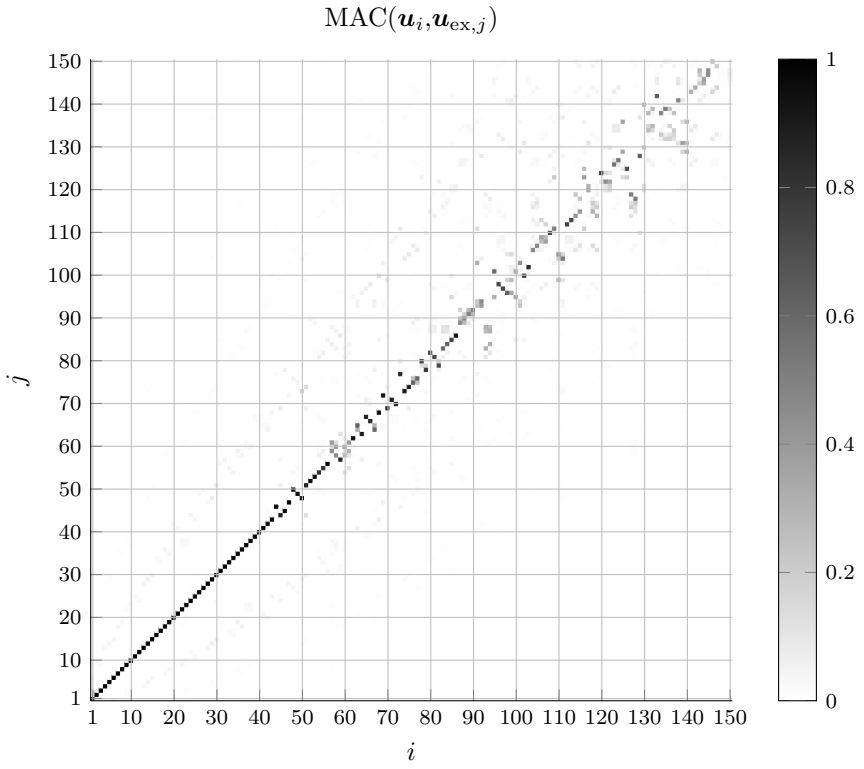

Figure 11: MAC matrix for the first 150 eigenmodes of a circular domain using second-order FEM (horizontal index) compared to the analytical eigenmodes (vertical index). From around mode 55, the numerical modes quickly start deteriorating.

approximation is 336, the modes shown thus go up to a normalised mode index of $i/N = 0.45$. This is a relatively lower region than is studied for the square domain, because the errors are for both FEM and IGA larger in the circular case and so the eigenmodes will also degenerate more rapidly. As is the case for the square domain, the lower modes are well approximated, up until almost the first 40 FE modes in this case. However, after that the mode accuracy decreases, especially beyond mode 60. The diagonal structure starts to fade, and above mode 130 few analytical modes seem to still be well represented by any of the numerically calculated ones. When solving a boundary value problem, the contribution of these higher modes is not incorporated properly because the mode shapes are not correctly represented, limiting the frequency range this model can be used for. The already decreasing accuracy of the eigenfrequencies in this region of the spectrum adds to this effect.

Figure 12 shows the corresponding MAC matrix when using 324 NURBS functions of second order. Although this model is slightly smaller than in the

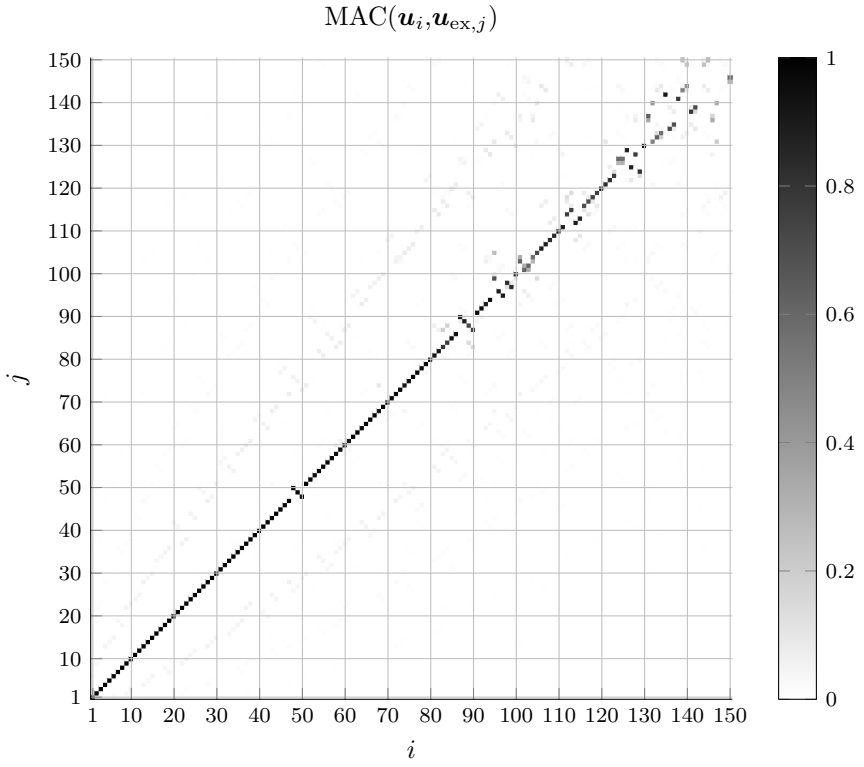

Figure 12: MAC matrix for the first 150 eigenmodes of a circular domain using second-order IGA (horizontal index) compared to the analytical eigenmodes (vertical index). The numerical IGA modes remain accurate much longer than the FE modes, allowing more efficient calculations toward higher frequencies.

FEM case, it approximates the mode shapes with a significantly higher accuracy: Aside from a few switched modes, the first 90 modes are accurately represented. And although the accuracy decreases with increasing mode number, the diagonal structure remains clearly visible up to mode 120. This shows that not only the eigenvalues are more accurately represented for the lower modes for IGA as compared to the FEM, also the eigenmodes are more closely approximated. For the sake of brevity, only second-order calculations are shown here, but similar conclusions can be drawn for higher-order shape functions.

Note that whereas in the square case the inaccuracies are mostly due to the switched order of appearance of the modes, the circular domain introduces more distortions in the mode shapes themselves, especially in the FEM case. Figure 13 illustrates this for modes 57 through 60 by comparing the FEM and the IGA mode shapes to the corresponding analytical ones. The FEM modes appear in the wrong order, i.e. modes 57 and 59 are switched. Additionally, even though the exact modes can be recognised in the FEM mode shapes, there are clear distortions present. These inaccuracies are also clearly expressed in

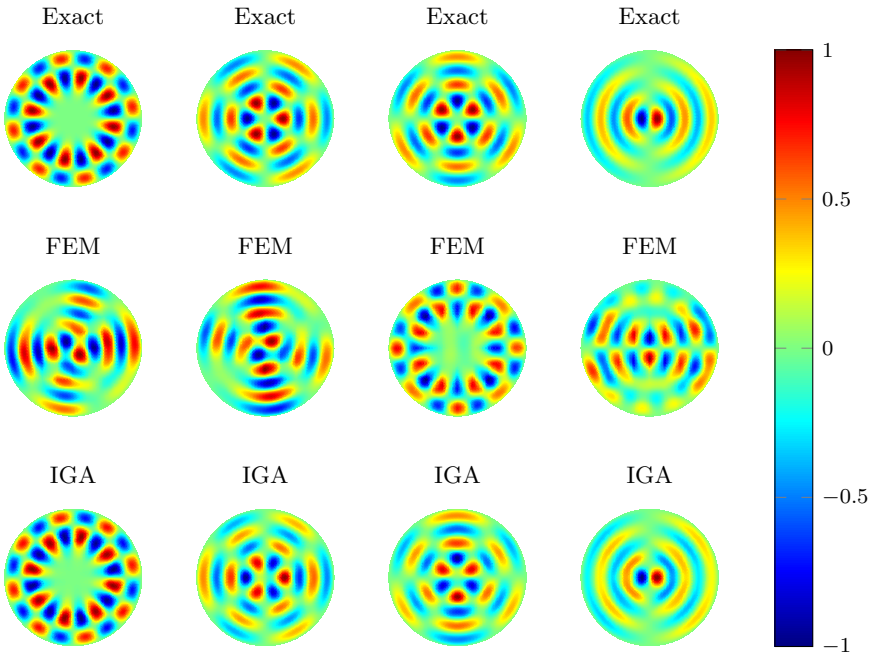

(a) 57^{th} mode $u_{82,\sin}(r,\theta)$ (b) 58^{th} mode $u_{34,\cos}(r,\theta)$ (c) 59^{th} mode $u_{34,\sin}(r,\theta)$ (d) 60^{th} mode $u_{15,\cos}(r,\theta)$

Figure 13: Analytical mode shapes number 57 through 60, as described by eqs. (19) and (20), compared to the corresponding numerically calculated modes with both FEM (cf. fig. 11) and IGA (cf. fig. 12). In contrast to the IGA mode shapes, the FEM ones appear in the wrong order and do not match the exact ones well.

fig. 11 by the rather low MAC values around mode 60. In contrast to this, the IGA modes appear in the correct order and match the exact ones very well.

5. Numerical verification studies

This section presents two numerical verification cases to confirm whether the findings previously derived from eigenvalue problems can also be extended to boundary value problems. First a relatively simple quadrilateral domain is studied. Convergence curves are shown for different frequencies of analysis, and the influence of the geometrical error is investigated into more detail. The second case study is a 2D car cavity consisting of multiple NURBS patches. This problem includes Robin boundary conditions to introduce a damping matrix and the acoustic response is studied over a wider frequency range. Also the accuracy of secondary variables is assessed.

5.1. Quadrilateral geometry

Consider the problem depicted in fig. 14 with governing equations (1) and (2b). The acoustic domain is excited by a unit normal velocity of the lower boundary while the other boundaries are rigid (i.e. zero normal velocity). All boundaries are described by biquadratic B-splines.

5.1.1. Convergence analysis

Several simulations are done using both IGA and FE models of various polynomial orders for calculating multiple frequency responses. In both cases, quadrilateral elements are used, as shown in the example meshes in fig. 15. The acoustic pressure response is evaluated in the 100 points indicated by red circles

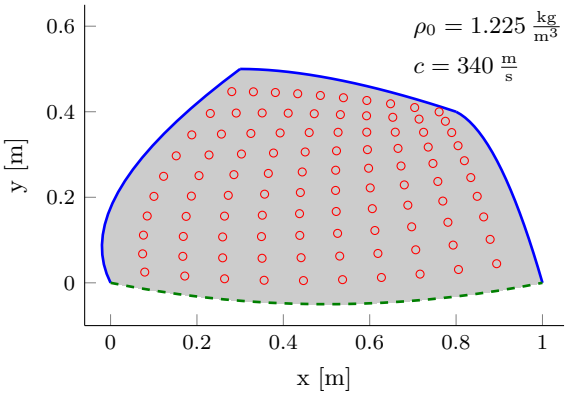

Figure 14: The bent quadrilateral geometry enclosed by 3 rigid boundaries (in solid blue) and excited by a unit normal velocity on the lower boundary (in dashed green). The red circles are the evaluation points used in the convergence study. The data defining the precise geometry is given in appendix in table 1.

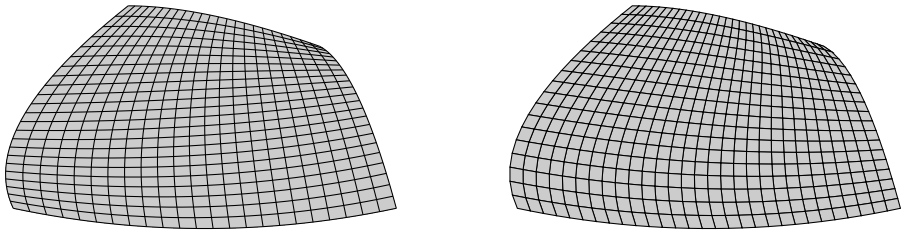

(a) Isogeometric mesh containing 529 quadratic B-spline elements.

(b) Finite element mesh containing 522 quadratic Lagrangian elements.

Figure 15: Meshes of the quadrilateral geometry generated using (a) quadratic B-splines and (b) quadratic polynomials.

in fig. 14. The discrete l^2 relative error norm $\|\epsilon\|_2$ is then calculated as follows using these 100 response points ($n_p = 100$):

$$\|\epsilon\|_2 = \frac{\|p_a(\boldsymbol{r}) - p_{a,\mathrm{ref}}(\boldsymbol{r})\|_2}{\|p_{a,\mathrm{ref}}(\boldsymbol{r})\|_2} = \frac{\sqrt{\sum_{i=1}^{n_p} |p_a(\boldsymbol{r_i}) - p_{a,\mathrm{ref}}(\boldsymbol{r_i})|^2}}{\sqrt{\sum_{i=1}^{n_p} |p_{a,\mathrm{ref}}(\boldsymbol{r_i})|^2}}, \tag{22}$$

where $p_{a,\mathrm{ref}}$ is the reference pressure response, in this case calculated with a cubic FE model with 460 000 DOFs.

Figure 16 plots this relative error versus the number of DOFs at a frequency of 250 Hz both for IGA and for FE models from polynomial order 1 to 5. Here

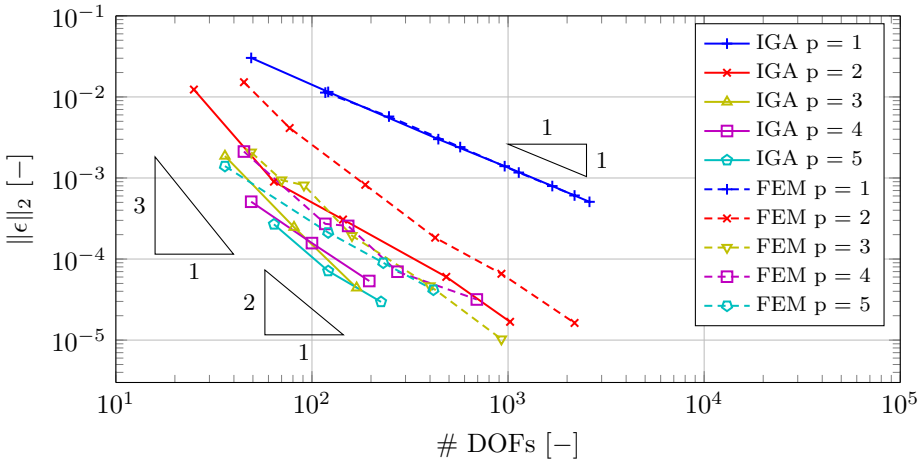

Figure 16: Convergence of IGA and FE models of various polynomial order p for the problem depicted in fig. 14 studied at 250 Hz. For a given model size and polynomial order, IGA is almost half an order of magnitude more accurate than the FEM at this frequency.

again the two linear models yield the same result, as the shape functions are in both cases identical. Looking at higher orders, it is clear that for a given number of DOFs, the IGA models are about half an order of magnitude more accurate than the FE models of the same polynomial order. The step from linear to quadratic shape functions yields the biggest accuracy gain. Elevating the order above cubic does not result in much additional accuracy. This is due to the relatively low frequency where the resulting pressure field is still rather simple and the higher order of the shape functions cannot add a lot of value to the already good lower-order approximations.

As the frequency increases, the pressure field becomes more complicated, as the contour plots in fig. 17 illustrate. More dynamic responses can be described more efficiently by the higher-order shape functions. Figure 18 shows the same convergence curves as in fig. 16 but now for a frequency of 1000 Hz. Here the step from cubic to quartic or quintic NURBS does improve the accuracy. Going to even higher frequencies would show the quartic and quintic IGA curves moving away from each other as well. It is also worth noting that to obtain the same accuracy at 1000 Hz as for 250 Hz, a finer model is necessary both for FEM and for IGA, because of the more complicated pressure field. When comparing IGA to FEM at this frequency, the superiority of IGA is even larger. Now more than an order of magnitude in accuracy is gained for a given order and number of DOFs when going from conventional polynomials to NURBS.

These results confirm the findings of section 4 that IGA models can analyse acoustic problems more efficiently than corresponding FE models, even more so as the frequency of analysis increases.

5.1.2. Influence of the geometrical error

An important advantage of IGA is that geometrical errors due to the discretisation can be avoided. In contrast to FEM, there is no need for going back to the original CAD description when refining the mesh, as already the most coarse parametrisation can exactly describe the geometry. The influence of the geometrical error for this problem is studied by starting from three initial first-order FE meshes and refining them without updating the initial geometrical

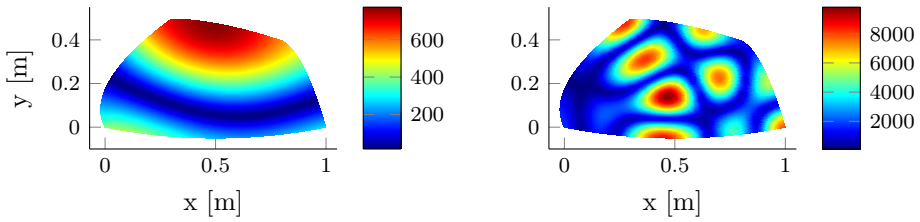

(a) Pressure response [Pa] at 250 Hz.

(b) Pressure response [Pa] at 1000 Hz.

Figure 17: Contour plots of the pressure responses in the quadrilateral geometry of fig. 14 at 250 and 1000 Hz, both computed using a quadratic IGA model containing 1024 DOFs.

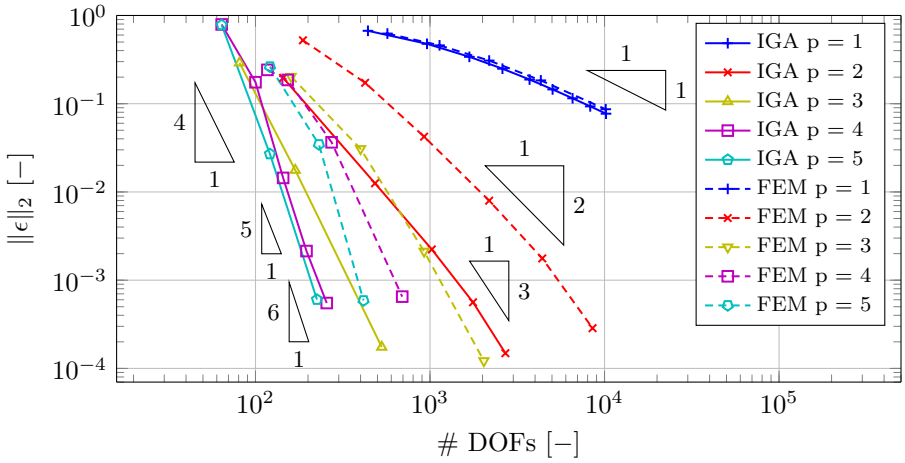

Figure 18: Convergence of IGA and FE models of varying order for the problem depicted in fig. 14 studied at 1000 Hz. This higher frequency makes the use of IGA models even more advantageous, with the higher-order IGA models outperforming the FEM by two orders of magnitude.

discretisation. Figure 19 shows the three initial geometries, referred to as X×Y with X and Y the original numbers of elements in x- and y-direction, respectively. Figure 20 illustrates what is meant by refining these models without refining the geometry.

These three models are used for calculating the acoustic response at 250 Hz. Figure 21 shows convergence plots, according to eq. (22), when refining the mesh without refining the geometry. For comparison purposes, the relative errors for the linear IGA and FE model with geometry refinement are also shown. The accuracy for the three models stagnates at an error level which is indicative of the geometrical error present in each model. To confirm this, these geometrical errors are calculated; they are given by the relative error ϵ_{SA} of the surface area (SA) of the starting geometries (cf. fig. 19) with respect to the exact surface

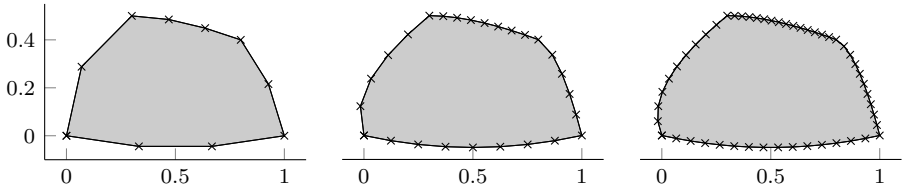

(a) split 3×2 (b) split 8×5 (c) split 15×10

Figure 19: The starting geometries for the FE models used to study the geometrical error in the problem depicted in fig. 14. The crosses indicate the vertices, which are linearly interpolated.

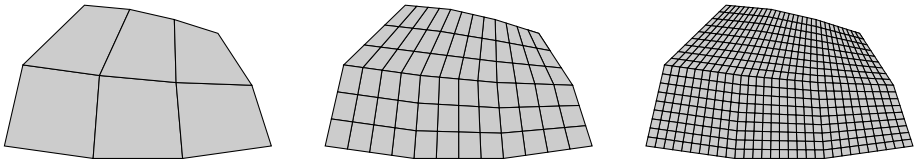

Figure 20: Three linear FE meshes generated from the split 3×2 model (cf. fig. 19a).

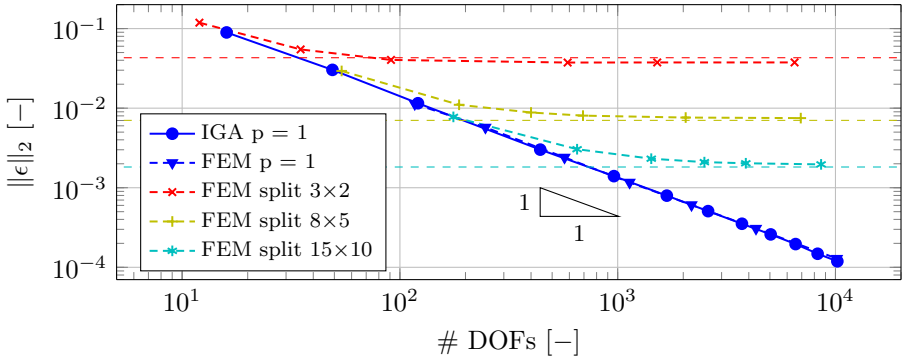

Figure 21: Convergence of FE models of various geometrically flawed meshes for the problem depicted in fig. 14 studied at 250 Hz. The geometrical errors present in these models (indicated by the horizontal dashed lines) clearly introduce a stagnation in accuracy.

area (cf. fig. 14): $\epsilon_{\text{SA}} = |\text{SA} - \text{SA}_{\text{exact}}|/\text{SA}_{\text{exact}}$. The coloured dashed lines in fig. 21 represent these geometrical error levels for each of the split models. They match the stagnated accuracies of the models well. Even the split 15×10 model, which visually seems to approximate the exact geometry already quite well, stagnates at a relatively large error value compared to the fully refined models. It should be noted that with increasing frequency, the geometrical error becomes more important: as higher-frequency waves diffract less easily, they are more sensitive to geometrical details.

5.2. Two-dimensional car cavity

This case study applies NURBS-based IGA to a more complex, multipatch geometry. Consider the two-dimensional car cavity depicted in fig. 22. The air inside the car is acoustically excited by a unit normal velocity applied to the firewall (in red), representing the transfer of engine vibrations through this panel. All boundaries are modelled as rigid (i.e. zero normal velocity), except for the seats, where a normal impedance $\bar{Z}_n$ is imposed (cf. eq. (2c)) to introduce acoustic absorption. In general, the acoustic impedance is a complex, frequency-dependent quantity, but for practical reasons a constant value is used here. The complex impedance introduces a damping matrix with complex entries into the system of equations (8), adding to the complexity of the problem.

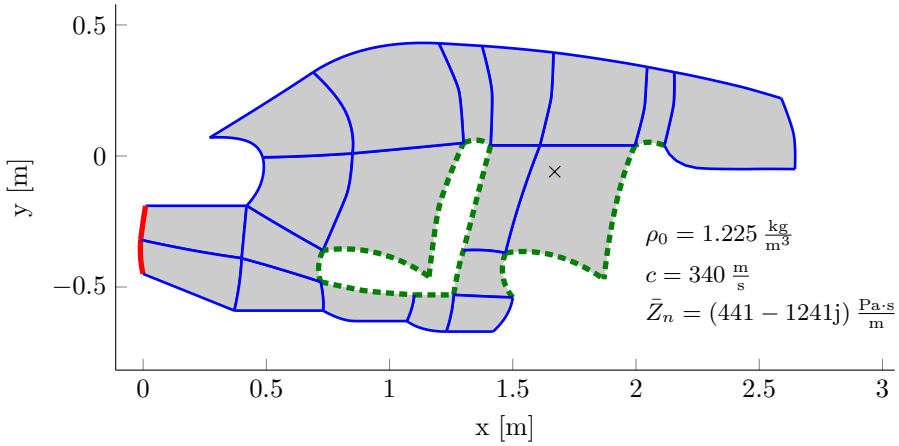

Figure 22: The multipatch 2D car cavity geometry, excited by a unit normal velocity of the firewall (solid red) with prescribed normal impedance on the seats (dashed green). The blue lines are the patch boundaries. The data defining the precise geometry is given in appendix in table 2.

As already mentioned in section 3.2, multiple bordering NURBS patches are by default discontinuous at the patch interfaces. To ensure continuity, conforming patches (i.e. with identical parametrisation at the interfaces) are used here. This has consequences for the geometry description that can be used. Not just any combination of patches is analysis-suitable, and care should be taken to generate a high-quality multipatch discretisation. Figure 22 shows the configuration of the 19 patches used here, with the blue lines in the interior of the domain indicating the interfaces. All patches are parametrised using biquadratic B-splines. They are C^1-continuous except at the patch interfaces, where there is only C^0 continuity.

The car cavity is studied in a frequency range from 10 to 2500 Hz with a frequency resolution of 2 Hz. Simulations are done using an IGA model consisting of 2846 quadratic DOFs and a FEM mesh containing 2867 quadratic DOFs. They are compared to a reference solution calculated using a quadratic FE model with 375 000 DOFs.

Figure 23 shows the acoustic pressure response curves in the point with coordinates (1.67 m; −0.06 m), indicated by the black cross in fig. 22. In the lower frequency region both the IGA and the FE calculation show good agreement with the reference. As the frequency increases, however, the curves start to shift to the right as compared to the reference as the resonance peaks shift to higher frequencies. This phenomenon is known as the pollution effect and is the result of accumulated phase errors due to numerical dispersion. It has been the subject of extensive research [16, 17, 46, 48] and is a prohibitive factor for using the FEM for very high-frequency calculations. Increasing the polynomial order reduces this effect but does not remove it. Figure 24 zooms in on

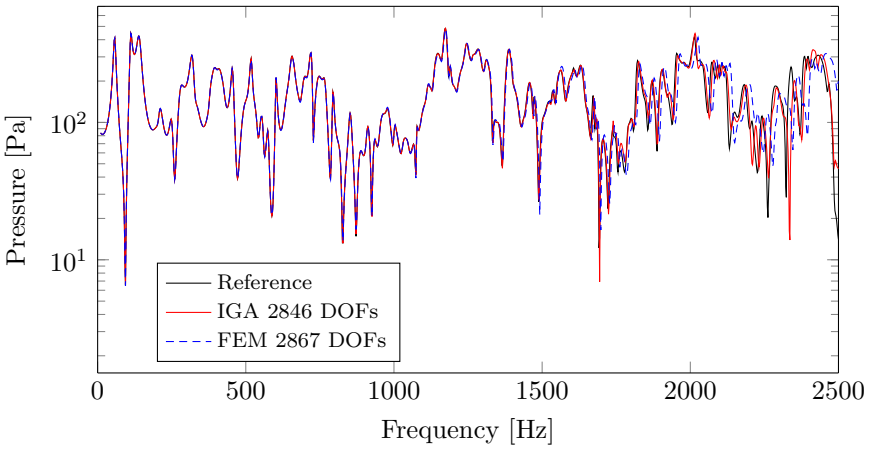

Figure 23: Pressure response curves for the point $(1.67\,\mathrm{m}; -0.06\,\mathrm{m})$ in the 2D car cavity, calculated with a quadratic IGA and a quadratic FE model. The FEM curve starts deviating from the reference more rapidly than the IGA one, indicating a more detrimental pollution effect in the FEM case.

the higher-frequency part of the acoustic response. This shows that although the IGA model also suffers from the pollution effect, it follows the reference up to higher frequencies than the FE discretisation does. The shift for the FEM curve already sets in at around 1400 Hz, while the IGA model only starts deteriorating around 1700 Hz. Increasing the frequency even further, this pollution effect clearly becomes stronger, although it does so less for the IGA model as compared to the FE model. This again confirms the findings from the previous sections, also for a complex problem setting.

Figure 25 shows the averaged relative error in the discrete l^2 norm $\|\epsilon\|_2$ (cf. eq. (22)) of the acoustic pressure in 76 evaluation points spread out over the entire car cavity (4 in each patch). Note that the complex values of the acoustic pressure are used in eq. (22), not simply the absolute ones. This means that also phase information is taken into account. This can be of importance here because, in contrast to the quadrilateral geometry studied in section 5.1, not all points are in phase with each other in this problem due to the impedance boundary condition. The figure illustrates that even for the lower frequencies the IGA model outperforms the FE discretisation. In the upper frequency region the difference becomes smaller and the error is large because of the pollution effect.

Evaluating secondary variables, such as the acoustic particle velocity, shows a similar gain in accuracy of IGA over FEM. Whereas C^0-continuous FEM shape functions result in discontinuous secondary variables, the higher continuity of NURBS yields smoother derived quantities.

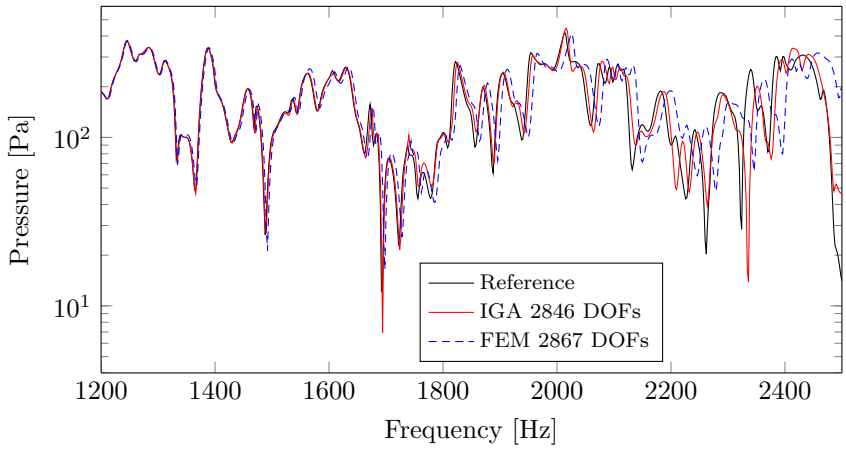

Figure 24: Close-up of fig. 23 between 1200 and 2500 Hz, more clearly showing the larger pollution effect in the FEM solution in comparison to the IGA model.

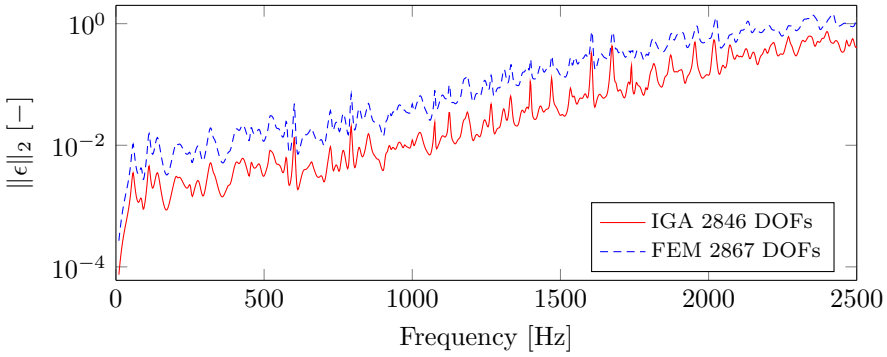

Figure 25: Averaged relative error of the pressure response over 76 points spread out over the car cavity, calculated using quadratic shape functions.

5.2.1. On the practical limitations of NURBS

Although this numerical case study illustrates the increased efficiency of NURBS-based IGA as compared to the conventional FEM, it is also a good demonstration of the limitations of using NURBS in more realistic (i.e. more geometrically complex) analysis cases. The main drawback is the tensor product structure. The straightforward use of conforming patches to ensure inter-patch continuity, without further treatment to allow for local refinement, means that refinements propagate from patch to patch. If a series of thus related patches change in size significantly from one patch to another, an unintentional and possibly undesired discrepancy in element sizes can occur. Comparing two different discretisations of the car cavity illustrates this issue.

Figures 26 and 27 show these two discretisations with different patch config-

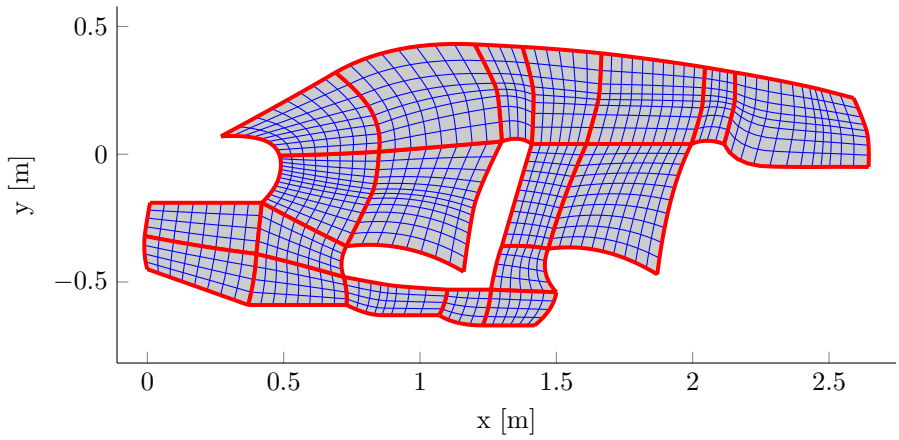

Figure 26: A B-spline discretisation of the car cavity topologically identical to the one used in the simulations. The blue lines delimit the elements, the red ones are the patch boundaries.

urations but with the same maximum element size. The one in fig. 26 is of the same topology (but larger element size) as the one that was used in the calculations discussed above. The deformation of the patches is limited and all the elements are of roughly the same size. The same cannot be said for the discretisation in fig. 27. Consider for instance the green patch. The element sizes there are determined by those in the yellow patches because of the use of conforming patches. The green patch therefore always contains finer elements than the yellow ones. This introduces elements that still contribute to the computational cost but that are too fine to contribute to the solution accuracy — because the latter is limited by the larger elements in other regions of the car cavity. The same reasoning holds also for other parts of the mesh.

This is of course not a new issue and although the cause is in essence the lack of local refinement possibilities in this framework, problems also arise in the case of uniform refinement of the entire mesh here. Whether this really poses a problem or not depends on the specific problem under study. It is mentioned here because simulations for the car cavity have indicated that this is indeed detrimental to the IGA efficiency and in very bad meshes can even cause the IGA model to be outperformed by the FEM on a per-DOF basis. More importantly, it undermines the primary purpose of IGA, namely rendering the meshing step in the FEM redundant. The care that has to be taken in dividing the problem domain into patches eventually boils down to a meshing process, but on a super-element level. Solutions for this problem exist, for instance in the form of geometrical technologies not suffering the tensor product issues of NURBS, such as T-splines, or of local refinement techniques [11, 35–37, 39, 40, 49]. Also hybrid techniques seem promising, such as the NURBS-enhanced FEM [50] or the blending of NURBS functions and local maximum entropy meshfree approximants [51]. In fact, the latter method has recently

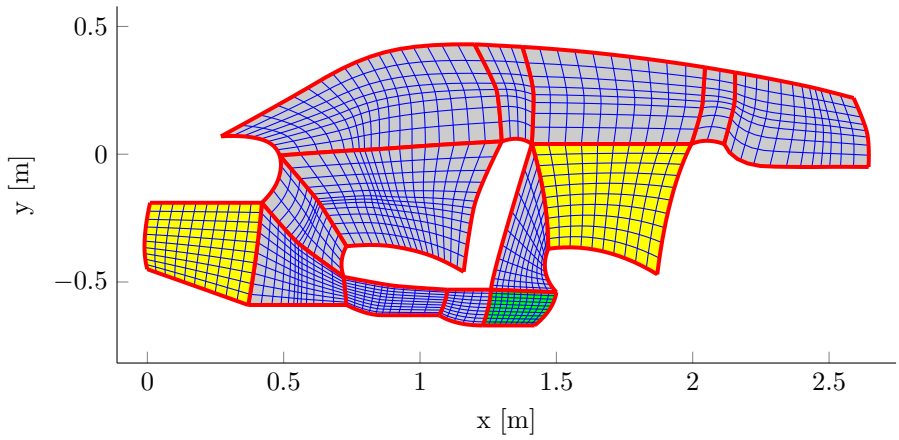

Figure 27: An example of a B-spline discretisation with a patch configuration inferior to the one in fig. 26 but with the same maximum element size. The blue lines delimit the elements, the red ones are the patch boundaries.

shown very positive results for time-harmonic acoustics in 2D, in particular with respect to pollution errors [52]. However, the existence of techniques like T-splines does not mean that the issue presented above is no longer relevant. The aim of the isogeometric paradigm is to directly plug in CAD descriptions into CAE environments, or in other words to change the analysis side while leaving the design side unaltered. The vast majority of CAD programmes is still NURBS-based. Applying isogeometric analysis would then ideally allow to directly use these NURBS in analysis environments, without requiring too many translation steps to more analysis-suitable geometries.

6. Conclusions

This work studies the performance of a NURBS-based isogeometric framework for solving stationary acoustic problems in two dimensions. A first assessment is done by studying the corresponding eigenvalue problem for simple domains with analytical solutions. It is shown that when using NURBS shape functions instead of conventional polynomials, not only the eigenvalue error increases less rapidly with increasing frequency, but also the mode shapes are represented more accurately. The increased accuracy over the extended lower-frequency part of the spectrum makes IGA more efficient than the FEM for calculating system responses, especially at higher frequencies. Two numerical case studies are done to further benchmark NURBS-based IGA versus the conventional FEM. A convergence analysis on a simple acoustic domain shows that IGA outperforms the FEM on a per-DOF basis. The higher the frequency of analysis, the larger the accuracy gain of IGA. The influence of the geometrical error is briefly studied, indicating the importance of using the exact geometry

when refining the mesh. Studying a multipatch car cavity geometry with absorbing boundaries over a wide frequency range confirms the findings that IGA can model stationary acoustics more efficiently than the conventional FEM. In particular in the higher frequency range, IGA seems to suffer less from the pollution effect than the FEM. Finally, the practical consequences of the inherent tensor product structure of NURBS are discussed. Without additional treatment, the propagation of refinement steps from patch to patch can compromise the efficiency of IGA calculations, and the care taken to produce a good multipatch discretisation could defeat the purpose of IGA as a bridge between CAD and CAE.

Acknowledgements

The research of Laurens Coox is funded by a PhD grant of the agency of Innovation by Science and Technology in Flanders (IWT-Flanders). Elke Deckers is a post-doctoral fellow of the Fund for Scientific Research – Flanders (FWO). The presented work is also supported by the Research Fund KU Leuven.

Appendix A. Geometrical problem data

This appendix lists the geometrical data necessary to recreate the problem domains studied in section 5. All domain boundaries are described by quadratic B-spline curves, defined by knot vectors and control points (cf. section 3):

$$C(\xi) = \sum_{i=1}^{n} N_i^p(\xi)\mathbf{B}_i, \tag{23}$$

with $N_i^p(\xi)$ from eq. (3) with $p = 2$.

A.1. Quadrilateral geometry

Table 1 presents the knot vectors and control points of the 4 quadratic B-spline segments forming the boundary of the quadrilateral geometry studied in section 5.1.

Table 1: Quadratic B-spline data defining the boundary segments describing the geometry in fig. 14.

Boundary	**Knot vector $\boldsymbol{\Xi}$** [-]	**Control points $\boldsymbol{B}_i$** [m]
1	$\boldsymbol{\Xi} = \{0, 0, 0, 1, 1, 1\}$	$\boldsymbol{B}_1 = (0.000, 0.000)$ $\boldsymbol{B}_2 = (-0.100, 0.200)$ $\boldsymbol{B}_3 = (0.300, 0.500)$
2	$\boldsymbol{\Xi} = \{0, 0, 0, 1, 1, 1\}$	$\boldsymbol{B}_1 = (1.000, 0.000)$ $\boldsymbol{B}_2 = (0.900, 0.350)$ $\boldsymbol{B}_3 = (0.800, 0.400)$
3	$\boldsymbol{\Xi} = \{0, 0, 0, 1, 1, 1\}$	$\boldsymbol{B}_1 = (0.000, 0.000)$ $\boldsymbol{B}_2 = (0.500, -0.100)$ $\boldsymbol{B}_3 = (1.000, 0.000)$
4	$\boldsymbol{\Xi} = \{0, 0, 0, 1, 1, 1\}$	$\boldsymbol{B}_1 = (0.300, 0.500)$ $\boldsymbol{B}_2 = (0.500, 0.500)$ $\boldsymbol{B}_3 = (0.800, 0.400)$

A.2. Two-dimensional car cavity

Table 2 presents the knot vectors and control points of the 32 quadratic B-spline segments forming the boundary of the two-dimensional car cavity studied in section 5.2.

Table 2: Quadratic B-spline data defining the boundary segments describing the geometry in fig. 22.

Boundary	**Knot vector $\boldsymbol{\Xi}$** [-]	**Control points $\boldsymbol{B}_i$** [m]
1	$\boldsymbol{\Xi} = \{0, 0, 0, 0.5, 1, 1, 1\}$	$\boldsymbol{B}_1 = (0.420, -0.190)$ $\boldsymbol{B}_2 = (0.469, -0.140)$ $\boldsymbol{B}_3 = (0.496, -0.042)$ $\boldsymbol{B}_4 = (0.485, -0.005)$
2	$\boldsymbol{\Xi} = \{0, 0, 0, 1, 1, 1\}$	$\boldsymbol{B}_1 = (0.270, 0.070)$ $\boldsymbol{B}_2 = (0.540, 0.225)$ $\boldsymbol{B}_3 = (0.690, 0.320)$
3	$\boldsymbol{\Xi} = \{0, 0, 0, 0.5, 1, 1, 1\}$	$\boldsymbol{B}_1 = (0.270, 0.070)$ $\boldsymbol{B}_2 = (0.358, 0.075)$ $\boldsymbol{B}_3 = (0.470, 0.043)$ $\boldsymbol{B}_4 = (0.485, -0.005)$
4	$\boldsymbol{\Xi} = \{0, 0, 0, \frac{1}{3}, \frac{2}{3}, 1, 1, 1\}$	$\boldsymbol{B}_1 = (2.590, 0.220)$ $\boldsymbol{B}_2 = (2.481, 0.251)$ $\boldsymbol{B}_3 = (2.415, 0.267)$ $\boldsymbol{B}_4 = (2.231, 0.307)$

– *continues on next page* –

Table 2 – *continued from previous page*

Boundary	**Knot vector $\boldsymbol{\Xi}$** [-]	**Control points $\boldsymbol{B}_i$** [m]
		$\boldsymbol{B}_5 = (2.155, 0.320)$
5	$\boldsymbol{\Xi} = \{0, 0, 0, \frac{1}{3}, \frac{2}{3}, 1, 1, 1\}$	$\boldsymbol{B}_1 = (2.645, -0.050)$ $\boldsymbol{B}_2 = (2.526, -0.049)$ $\boldsymbol{B}_3 = (2.414, -0.051)$ $\boldsymbol{B}_4 = (2.151, -0.046)$ $\boldsymbol{B}_5 = (2.115, 0.040)$
6	$\boldsymbol{\Xi} = \{0, 0, 0, 0.5, 1, 1, 1\}$	$\boldsymbol{B}_1 = (2.590, 0.220)$ $\boldsymbol{B}_2 = (2.626, 0.134)$ $\boldsymbol{B}_3 = (2.649, 0.049)$ $\boldsymbol{B}_4 = (2.645, -0.050)$
7	$\boldsymbol{\Xi} = \{0, 0, 0, 1, 1, 1\}$	$\boldsymbol{B}_1 = (2.155, 0.320)$ $\boldsymbol{B}_2 = (2.100, 0.330)$ $\boldsymbol{B}_3 = (2.045, 0.340)$
8	$\boldsymbol{\Xi} = \{0, 0, 0, 1, 1, 1\}$	$\boldsymbol{B}_1 = (2.115, 0.040)$ $\boldsymbol{B}_2 = (2.050, 0.065)$ $\boldsymbol{B}_3 = (1.995, 0.040)$
9	$\boldsymbol{\Xi} = \{0, 0, 0, 1, 1, 1\}$	$\boldsymbol{B}_1 = (1.665, 0.395)$ $\boldsymbol{B}_2 = (1.855, 0.372)$ $\boldsymbol{B}_3 = (2.045, 0.340)$
10	$\boldsymbol{\Xi} = \{0, 0, 0, 1, 1, 1\}$	$\boldsymbol{B}_1 = (1.995, 0.040)$ $\boldsymbol{B}_2 = (1.908, -0.145)$ $\boldsymbol{B}_3 = (1.870, -0.470)$
11	$\boldsymbol{\Xi} = \{0, 0, 0, 1, 1, 1\}$	$\boldsymbol{B}_1 = (1.470, -0.370)$ $\boldsymbol{B}_2 = (1.670, -0.340)$ $\boldsymbol{B}_3 = (1.870, -0.470)$
12	$\boldsymbol{\Xi} = \{0, 0, 0, 1, 1, 1\}$	$\boldsymbol{B}_1 = (1.375, 0.420)$ $\boldsymbol{B}_2 = (1.500, 0.413)$ $\boldsymbol{B}_3 = (1.665, 0.395)$
13	$\boldsymbol{\Xi} = \{0, 0, 0, 1, 1, 1\}$	$\boldsymbol{B}_1 = (1.300, 0.050)$ $\boldsymbol{B}_2 = (1.365, 0.075)$ $\boldsymbol{B}_3 = (1.410, 0.040)$
14	$\boldsymbol{\Xi} = \{0, 0, 0, 1, 1, 1\}$	$\boldsymbol{B}_1 = (1.200, 0.430)$ $\boldsymbol{B}_2 = (1.293, 0.425)$ $\boldsymbol{B}_3 = (1.375, 0.420)$
15	$\boldsymbol{\Xi} = \{0, 0, 0, 1, 1, 1\}$	$\boldsymbol{B}_1 = (1.410, 0.040)$ $\boldsymbol{B}_2 = (1.365, -0.120)$ $\boldsymbol{B}_3 = (1.300, -0.360)$
16	$\boldsymbol{\Xi} = \{0, 0, 0, 1, 1, 1\}$	$\boldsymbol{B}_1 = (1.500, -0.540)$ $\boldsymbol{B}_2 = (1.435, -0.465)$ $\boldsymbol{B}_3 = (1.470, -0.370)$
17	$\boldsymbol{\Xi} = \{0, 0, 0, 1, 1, 1\}$	$\boldsymbol{B}_1 = (1.260, -0.530)$ $\boldsymbol{B}_2 = (1.280, -0.415)$

– *continues on next page* –

Table 2 – *continued from previous page*

Boundary	**Knot vector $\boldsymbol{\Xi}$** [-]	**Control points $\boldsymbol{B}_i$** [m]
		$\boldsymbol{B}_3$ = (1.300, -0.360)
18	$\boldsymbol{\Xi}$ = {0, 0, 0, 1, 1, 1}	$\boldsymbol{B}_1$ = (1.230, -0.670) $\boldsymbol{B}_2$ = (1.335, -0.670) $\boldsymbol{B}_3$ = (1.420, -0.670)
19	$\boldsymbol{\Xi}$ = {0, 0, 0, 1, 1, 1}	$\boldsymbol{B}_1$ = (1.500, -0.540) $\boldsymbol{B}_2$ = (1.490, -0.610) $\boldsymbol{B}_3$ = (1.420, -0.670)
20	$\boldsymbol{\Xi}$ = {0, 0, 0, 1, 1, 1}	$\boldsymbol{B}_1$ = (1.100, -0.530) $\boldsymbol{B}_2$ = (1.180, -0.530) $\boldsymbol{B}_3$ = (1.260, -0.530)
21	$\boldsymbol{\Xi}$ = {0, 0, 0, 1, 1, 1}	$\boldsymbol{B}_1$ = (1.070, -0.630) $\boldsymbol{B}_2$ = (1.130, -0.670) $\boldsymbol{B}_3$ = (1.230, -0.670)
22	$\boldsymbol{\Xi}$ = {0, 0, 0, 0.5, 1, 1, 1}	$\boldsymbol{B}_1$ = (0.720, -0.480) $\boldsymbol{B}_2$ = (0.838, -0.504) $\boldsymbol{B}_3$ = (0.928, -0.519) $\boldsymbol{B}_4$ = (1.100, -0.530)
23	$\boldsymbol{\Xi}$ = {0, 0, 0, 0.5, 1, 1, 1}	$\boldsymbol{B}_1$ = (0.730, -0.590) $\boldsymbol{B}_2$ = (0.805, -0.630) $\boldsymbol{B}_3$ = (0.915, -0.630) $\boldsymbol{B}_4$ = (1.070, -0.630)
24	$\boldsymbol{\Xi}$ = {0, 0, 0, 0.5, 1, 1, 1}	$\boldsymbol{B}_1$ = (1.160, -0.460) $\boldsymbol{B}_2$ = (1.182, -0.284) $\boldsymbol{B}_3$ = (1.212, -0.139) $\boldsymbol{B}_4$ = (1.300, 0.050)
25	$\boldsymbol{\Xi}$ = {0, 0, 0, 1, 1, 1}	$\boldsymbol{B}_1$ = (1.160, -0.460) $\boldsymbol{B}_2$ = (0.955, -0.330) $\boldsymbol{B}_3$ = (0.730, -0.360)
26	$\boldsymbol{\Xi}$ = {0, 0, 0, 1, 1, 1}	$\boldsymbol{B}_1$ = (1.200, 0.430) $\boldsymbol{B}_2$ = (0.895, 0.445) $\boldsymbol{B}_3$ = (0.690, 0.320)
27	$\boldsymbol{\Xi}$ = {0, 0, 0, 1, 1, 1}	$\boldsymbol{B}_1$ = (0.420, -0.190) $\boldsymbol{B}_2$ = (0.225, -0.190) $\boldsymbol{B}_3$ = (0.010, -0.190)
28	$\boldsymbol{\Xi}$ = {0, 0, 0, 1, 1, 1}	$\boldsymbol{B}_1$ = (0.010, -0.190) $\boldsymbol{B}_2$ = (0.000, -0.245) $\boldsymbol{B}_3$ = (-0.010, -0.320)
29	$\boldsymbol{\Xi}$ = {0, 0, 0, 1, 1, 1}	$\boldsymbol{B}_1$ = (0.000, -0.450) $\boldsymbol{B}_2$ = (-0.015, -0.395) $\boldsymbol{B}_3$ = (-0.010, -0.320)
30	$\boldsymbol{\Xi}$ = {0, 0, 0, 1, 1, 1}	$\boldsymbol{B}_1$ = (0.370, -0.590) $\boldsymbol{B}_2$ = (0.160, -0.510)

– *continues on next page* –

Table 2 – *continued from previous page*

Boundary	**Knot vector $\boldsymbol{\Xi}$** [-]	**Control points $\boldsymbol{B}_i$** [m]
		$\boldsymbol{B}_3$ = (0.000, -0.450)
31	$\boldsymbol{\Xi}$ = {0, 0, 0, 1, 1, 1}	$\boldsymbol{B}_1$ = (0.730, -0.590) $\boldsymbol{B}_2$ = (0.550, -0.590) $\boldsymbol{B}_3$ = (0.370, -0.590)
32	$\boldsymbol{\Xi}$ = {0, 0, 0, 1, 1, 1}	$\boldsymbol{B}_1$ = (0.730, -0.360) $\boldsymbol{B}_2$ = (0.700, -0.420) $\boldsymbol{B}_3$ = (0.720, -0.480)

References

[1] O. Zienkiewicz, R. Taylor, The Finite Element Method — The Three Volume Set, 6th Edition, Butterworth-Heinemann, 2005.

[2] L. Thompson, A review of finite-element methods for time-harmonic acoustics, Journal of the Acoustical Society of America 119 (2006) 1315–1330.

[3] P. Banerjee, R. Butterfield, Boundary element methods in engineering science, McGraw-Hill, London, 1981.

[4] T. Wu, Boundary Element Acoustics, Fundamentals and Computer Codes, WIT Press, 2000.

[5] M. Vorlander, Simulation of the transient and steady-state sound propagation in rooms using a new combined ray-tracing/image-source algorithm, The Journal of the Acoustical Society of America 86 (1989) 172–178.

[6] R. Lyon, R. DeJong, Theory and Application of Statistical Energy Analysis, 2nd Edition, Butterworth-Heinemann, 1994.

[7] P. Frey, P. George, Mesh Generation, ISTE, Wiley, 2010.

[8] T. Hughes, J. Cottrell, Y. Bazilevs, Isogeometric analysis: CAD, finite elemens, NURBS, exact geometry and mesh refinement, Computer Methods in Applied Mechanics and Engineering 194 (2005) 4135–4195.

[9] W. Wall, M. Frenzel, C. Cyron, Isogeometric structural shape optimization, Computer Methods in Applied Mechanics and Engineering 197 (2008) 2976–2988.

[10] D. Fuβeder, B. Simeon, A.-V. Vuong, Fundamental aspects of shape optimization in the context of isogeometric analysis, Computer Methods in Applied Mechanics and Engineering 286 (2015) 313–331.

[11] M. Scott, R. Simpson, J. Evans, S. Bordas, T. Hughes, T. Sederberg, Isogeometric boundary element analysis using unstructured T-splines, Computer Methods in Applied Mechanics and Engineering 254 (2013) 197–221.

[12] R. Simpson, M. Scott, M. Taus, D. Thomas, H. Lian, Acoustic isogeometric boundary element analysis, Computer Methods in Applied Mechanics and Engineering 269 (2014) 265–290.

[13] H. Lian, R. Simpson, S. Bordas, Stress analysis without meshing: isogeometric boundary element method, Proceedings of the Istitution of Civil Engineers - Engineering and Computational Mechanics 166 (2013) 88–99.

[14] L. Coox, O. Atak, D. Vandepitte, W. Desmet, An isogeometric indirect boundary element method for solving acoustic problems in open-boundary domains, Computer Methods in Applied Mechanics and Engineering. *Under review.*

[15] K. Kostas, A. Ginnis, C. Politis, P. Kaklis, Ship-hull shape optimization with a T-spline based BEM-isogeometric solver, Computer Methods in Applied Mechanics and Engineering 284 (2015) 611–622.

[16] F. Ihlenburg, I. Babuška, Finite Element Solution of the Helmholtz Equation with High Wave Number Part II: The h-p-Version of the FEM, SIAM Journal of Numerical Analysis 34 (1997) 315–358.

[17] A. Deraemaeker, I. Babuška, P. Bouillard, Dispersion and pollution of the FEM solution for the Helmholtz equation in one, two and three dimensions, International Journal for Numerical Methods in Engineering 46 (1999) 471–499.

[18] P. Bouillard, F. Ihlenburg, Error estimation and adaptivity for the finite element method in acoustics: 2D and 3D applications, Computer Methods in Applied Mechanics and Engineering 176 (1999) 147–163.

[19] T. Strouboulis, K. Copps, I. Babuška, The generalized finite element method, Computer Methods in Applied Mechanics and Engineering 190 (2001) 4081–4193.

[20] E. Deckers, O. Atak, L. Coox, R. D'Amico, H. Devriendt, J. S., K. Koo, B. Pluymers, D. Vandepitte, W. Desmet, The wave based method: An overview of 15 years of research, Wave Motion 51 (2014) 550–565.

[21] P. Rouch, P. Ladevèze, The variational theory of complex rays: a predictive tool for medium-frequency vibrations, Computer Methods in Applied Mechanics and Engineering 192 (2003) 3301–3315.

[22] J. Cottrell, T. Hughes, Y. Bazilevs, Isogeometric Analysis: Toward Integration of CAD and FEA, John Wiley & Sons, 2009.

[23] Y. Bazilevs, L. Beirão da Veiga, J. Cottrell, T. Hughes, G. Sangalli, Isogeometric Analysis: approximation, stability and error estimates for h-refined meshes, Mathematical Models and Methods in Applied Sciences 16 (2006) 1031–1090.

[24] J. Evans, Y. Bazilevs, I. Babuška, T. Hughes, n-Widths, sup-infs, and optimality ratios for the k-version of the isogeometric finite element method, Computer Methods in Applied Mechanics and Engineering 198 (2009) 1726–1741.

[25] T. Hughes, J. Evans, A. Reali, Finite element and NURBS approximations of eigenvalue, boundary-value and initial-value problems, Computational Methods in Applied Mechanical Engineering 272 (2014) 290–320.

[26] V. P. Nguyen, C. Anitescu, S. P. Bordas, T. Rabczuk, Isogeometric analysis: an overview and computer implementation aspects, Mathematics and Computers in Simulation 117 (2015) 89–116.

[27] L. Coox, O. Atak, D. Vandepitte, W. Desmet, An isogeometric indirect boundary element method for Helmholtz problems, in: Proceedings of the 26th Conference on Noise and Vibration Engineering (ISMA2014), 2014, pp. 4189 – 4201.

[28] T. Hughes, A. Reali, G. Sangalli, Duality and unified analysis of discrete approximations in structural dynamics and wave propagation: Comparison of p-method finite elements with k-method NURBS, Computer Methods in Applied Mechanics and Engineering 197 (49–50) (2008) 4104–4124.

[29] J. Cottrell, A. Reali, Y. Bazilevs, T. Hughes, Isogeometric analysis of structural vibrations, Computer Methods in Applied Mechanics and Engineering 195 (2006) 5257–5296.

[30] P. Morse, K. Ingard, Theoretical Acoustics, Princeton University Press, 1968.

[31] L. Piegl, W. Tiller, The NURBS Book, Springer-Verlag Berlin Heidelberg, 1997.

[32] M. Cox, The numerical evaluation of B-splines, DNAC 4, National Physics Laboratory (1971).

[33] C. de Boor, On calculation with B-splines, Journal of Approximation Theory 6 (1972) 50–62.

[34] J. Cottrell, T. Hughes, A. Reali, Studies of refinement and continuity in isogeometric structural analysis, Computer Methods in Applied Mechanics and Engineering 196 (2007) 4160–4183.

[35] S. K. Kleiss, B. Jüttler, W. Zulehner, Enhancing isogeometric analysis by a finite element-based local refinement strategy, Computer Methods in Applied Mechanics and Engineering 213–216 (2012) 168–182.

[36] A. Vuong, C. Giannelli, B. Jüttler, B. Simeon, A hierarchical approach to adaptive local refinement in isogeometric analysis, Computer Methods in Applied Mechanics and Engineering 200 (2011) 3354–3567.

[37] D. Schillinger, E. Rank, An unfitted hp-adaptive finite element method based on hierarchical B-splines for interface problems of complex geometry, Computer Methods in Applied Mechanics and Engineering 200 (2011) 3358–3380.

[38] T. Sederberg, J. Zhen, A. Bakenov, A. Nasri, T-splines and T-NURCCs, ACM Transactions on Graphics 22 (3) (2003) 477–484.

[39] Y. Bazilevs, V. Calo, J. Cottrell, J. Evans, T. Hughes, L. S., M. Scott, T. Sederberg, Isogeometric analysis using T-splines, Computer Methods in Applied Mechanics and Engineering 199 (2010) 229–263.

[40] M. Scott, X. Li, T. Sederberg, T. Hughes, Local refinement of analysis-suitable T-splines, Computer Methods in Applied Mechanics and Engineering 213 (2012) 206–222.

[41] B. Marussig, J. Zechner, G. Beer, T.-P. Fries, Fast isogeometric boundary element method based on independent field approximation, Computer Methods in Applied Mechanics and Engineering 284 (2015) 458–488.

[42] G. Xu, E. Atroshchenko, S. Bordas, Geometry-Independent Field approximaTion: CAD-Analysis Integration, geometrical exactness and adaptivity, in: Proceedings of the 11th World Congress in Computational Mechanics, 2014.

[43] C. de Falco, A. Reali, R. Vázquez, GeoPDEs: a research tool for Isogeometric Analysis of PDEs, Advances in Engineering Software 42 (2011) 1020–1034.
URL http://geopdes.sourceforge.net/

[44] COMSOL Multiphysics.
URL http://www.comsol.com/comsol-multiphysics

[45] J. W. Brown, R. V. Churchill, Fourier Series and Boundary Value Problems, McGraw-Hill, 1993.

[46] F. Ihlenburg, I. Babuška, Finite Element Solution of the Helmholtz Equation with High Wave Number Part I: The h-Version of the FEM, Computers & Mathematics with Applications 30 (1995) 9–37.

[47] W. Heylen, S. Lammens, P. Sas, Modal Analysis Theory and Testing, Katholieke Universiteit Leuven – Departement Werktuigkunde, 2007.

[48] S. Esterhazy, J. Melenk, An analysis of discretizations of the Helmholtz equation in L^2 and in negative norms, Computers & Mathematics with Applications 67 (2014) 830–853.

[49] D. Schillinger, L. Dedè, M. A. Scott, J. A. Evans, M. J. Borden, E. Rank, T. J. Hughes, An isogeometric design-through-analysis methodology based on adaptive hierarchical refinement of NURBS, immersed boundary methods, and T-spline CAD surfaces, Computer Methods in Applied Mechanics and Engineering 249–252 (2012) 116–150.

[50] R. Sevilla, F.-M. S., A. Huerta, NURBS-enhanced finite element method (NEFEM), International Journal for Numerical Methods in Engineering 76 (2011) 56–83.

[51] A. Rosolen, M. Arroyo, Blending isogeometric analysis and local maximum entropy meshfree approximants, Computer Methods in Applied Mechanics and Engineering 264 (2013) 95–107.

[52] F. Greco, L. Coox, W. Desmet, Maximum-entropy methods for time-harmonic acoustics, Computer Methods in Applied Mechanics and Engineering. *Under review.*